Lecture 6

CME Energetics

February 6, 2017

early observations and models of CMEs

CMEs observed during solar eclipses, and by Mauna Loa and SMM, showing their three-part structure. (Hundhausen et al, 80-90s, Low, Gibson et al., Low 1996).

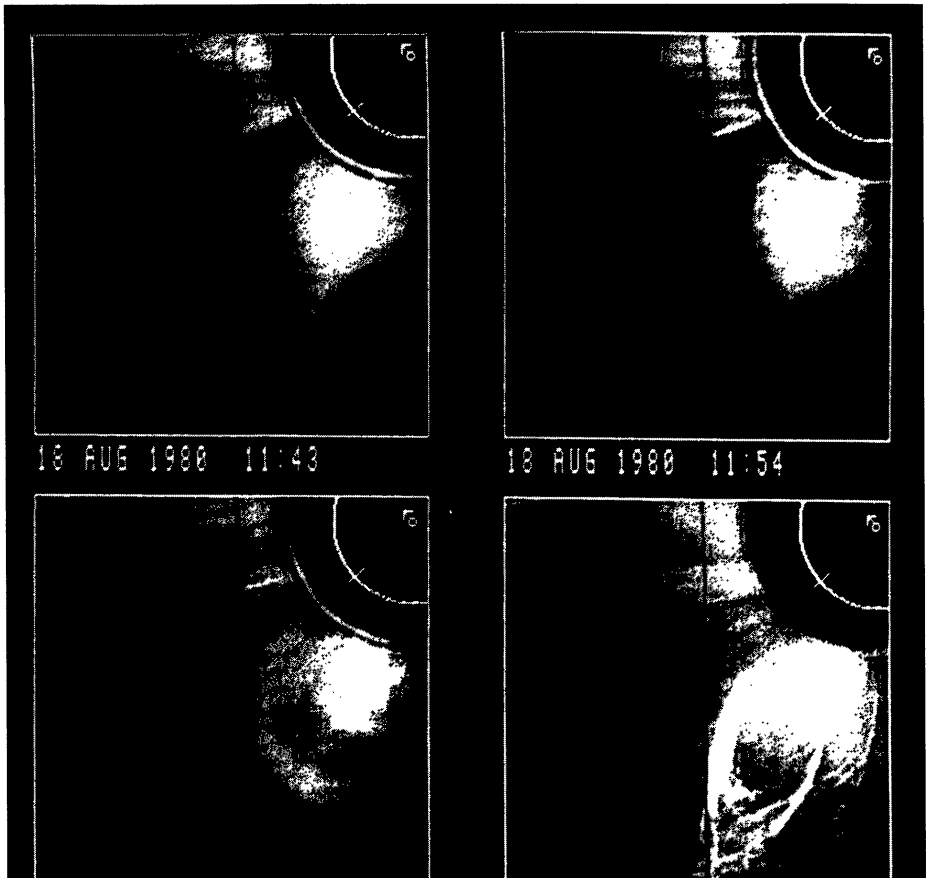

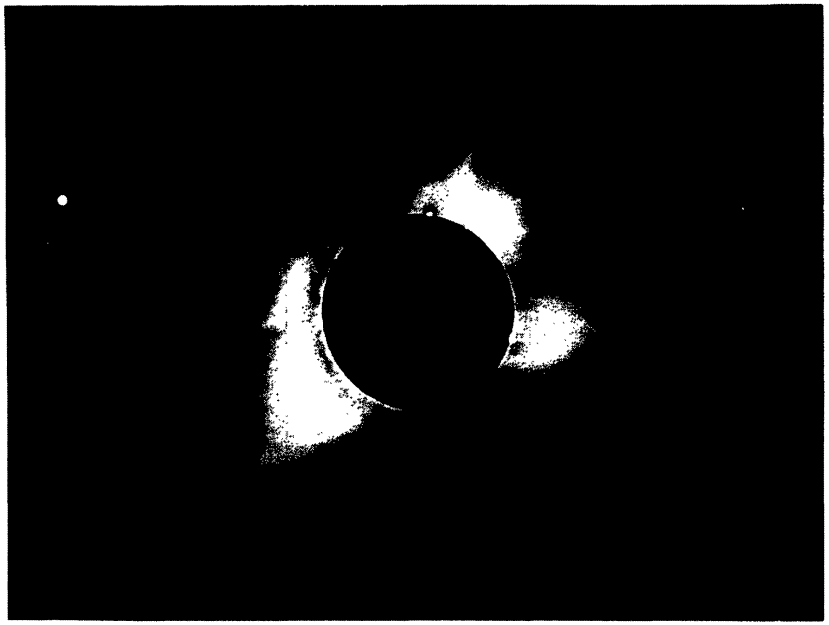

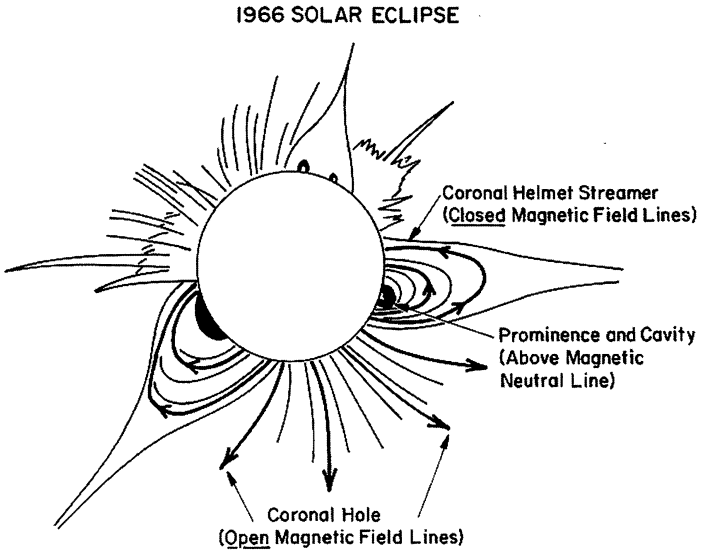

Figure 1. Photograph of the 1974 total eclipse showing the white-light corona with a sketch of the large-scale coronal magnetic lines of force taken from Hundhausen (1994). The lines of force in the

modern coronagraphs observing CMEs

Large Angle and Spectrometric COronagraph (LASCO, 1995 -) observes CMEs from earth view, with the FOV in solar radii:

C1: 1.1 - 3 ,

C2: 1.5 - 6,

C3: 3.5 - 30

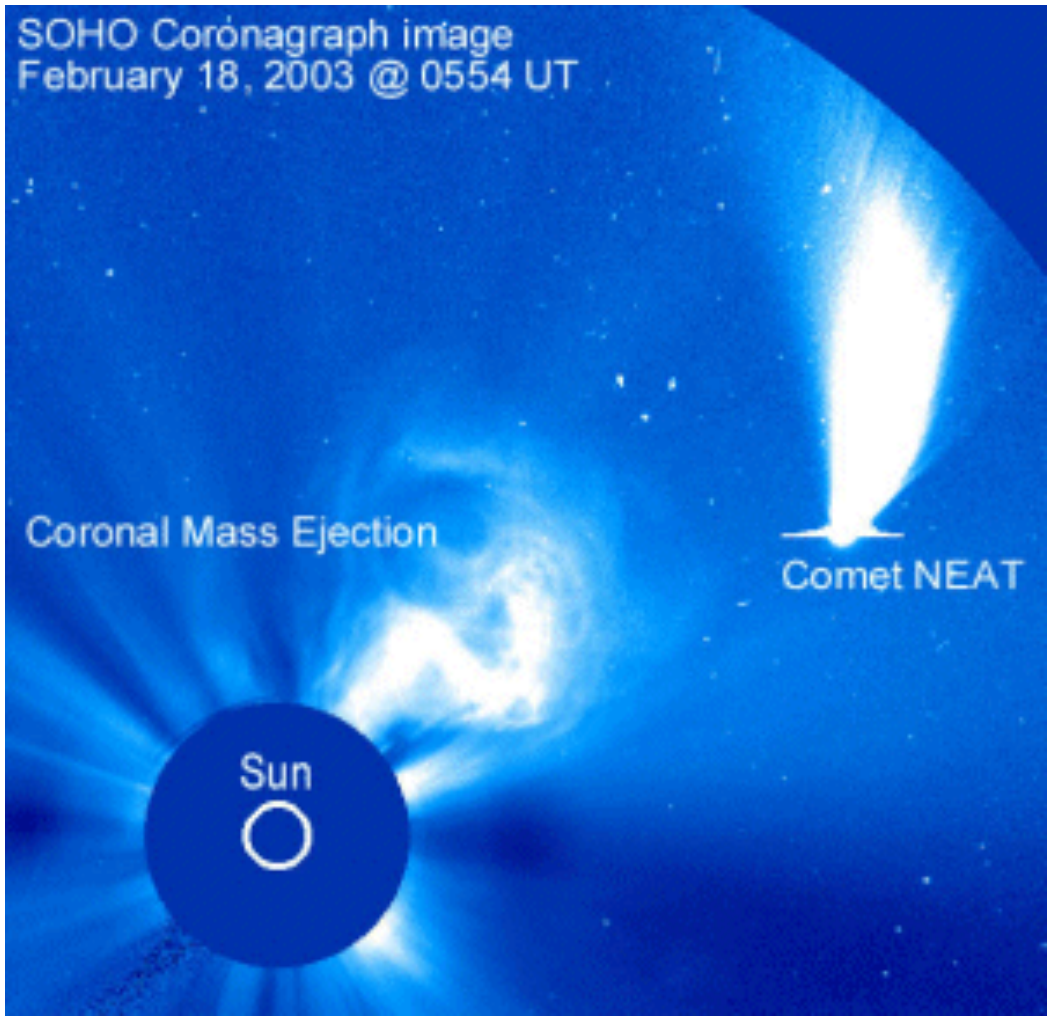

modern coronagraphs observing CMEs

STEREO (2006 -) carries EUVI (0 – 1.7), COR1 (1.5– 4), COR2 (- 15), HI (- 1AU) instruments in a twin spacecraft A and B.

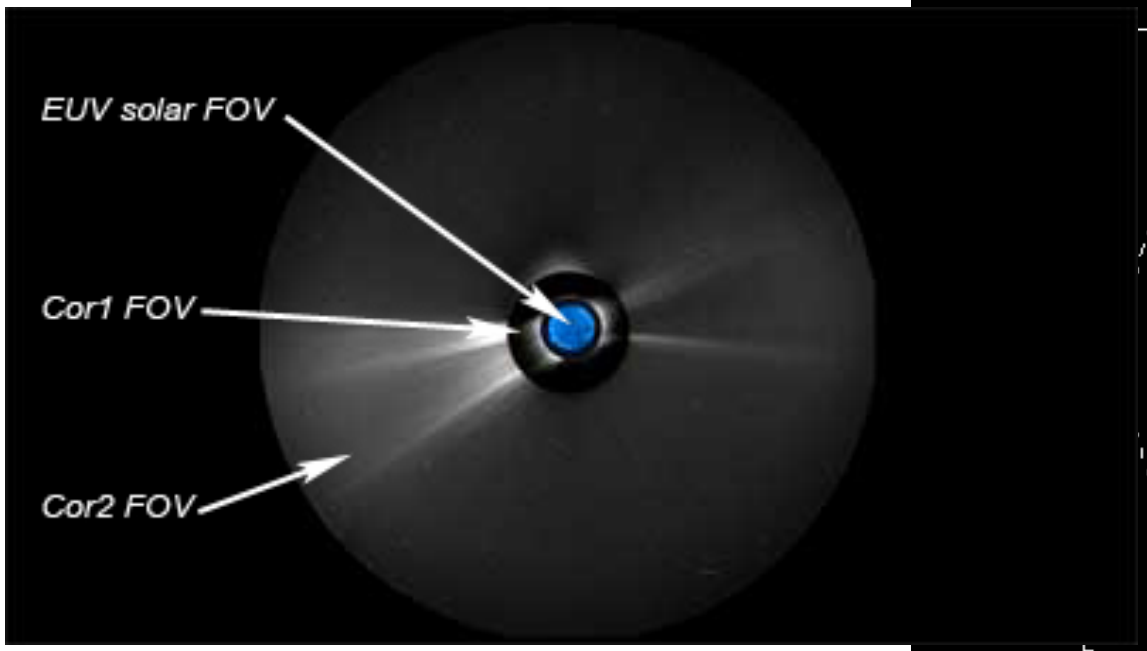

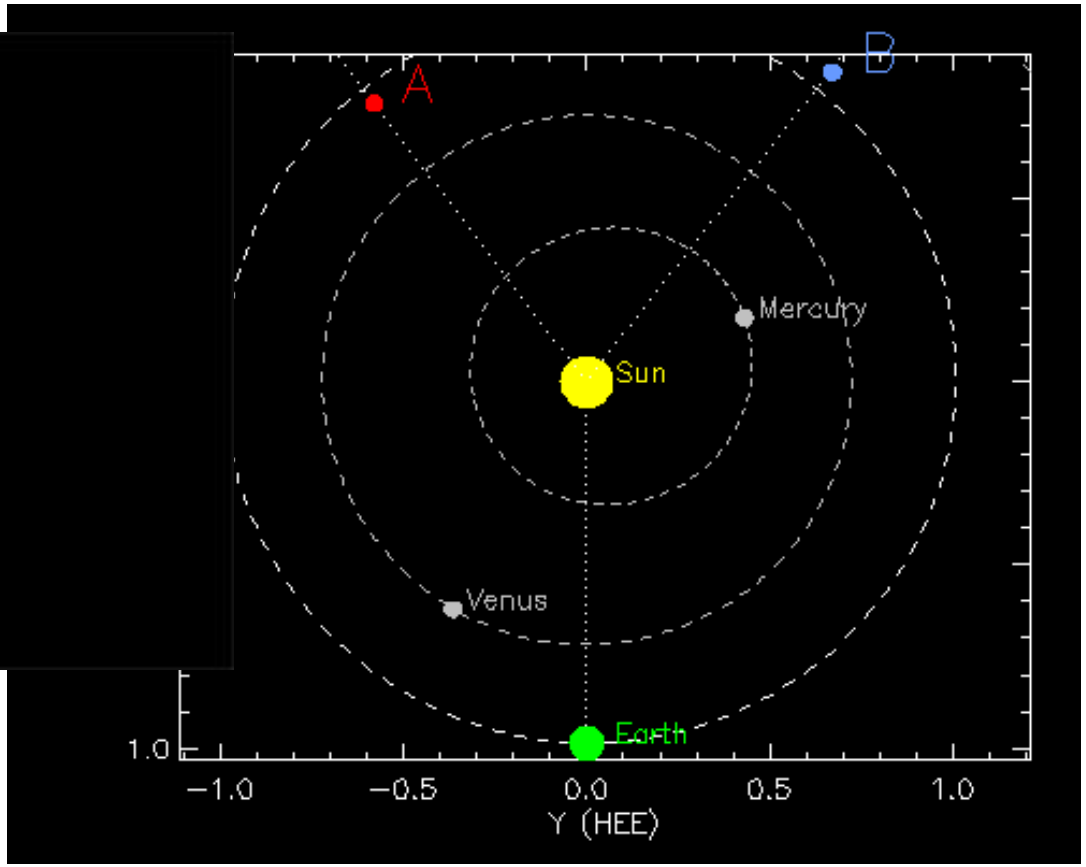

Where is STEREO today?

the three-part white light CME

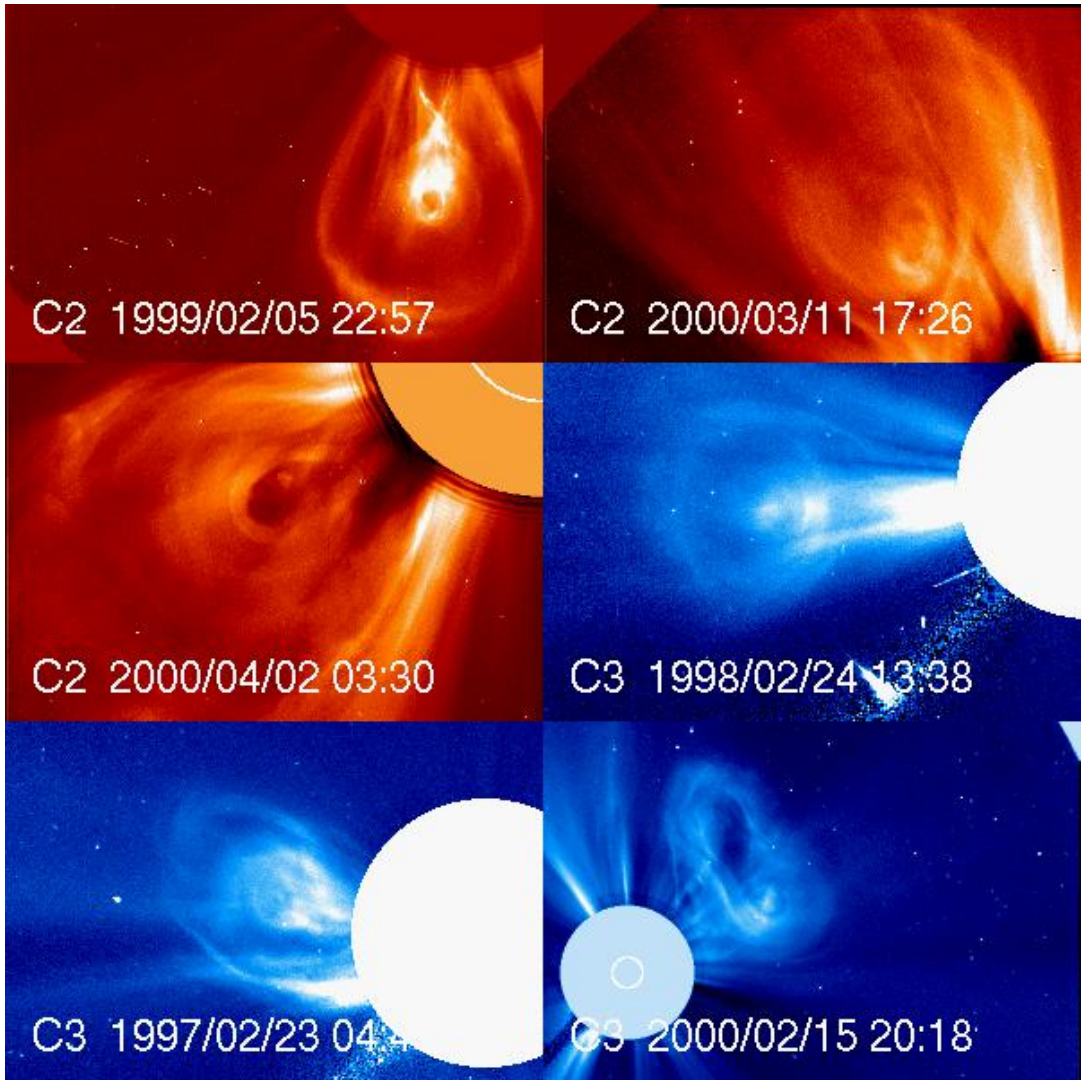

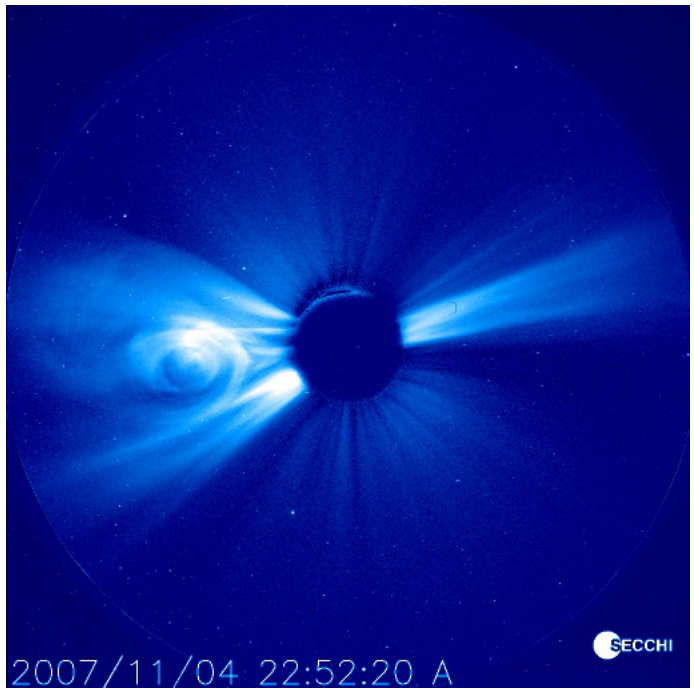

Mass and velocity are measured in white-light images.

mass and energy of CMEs

$$E = \frac{1}{2}Mv^2 + \frac{1}{2}Mv_{esc}^2\left(1 - \frac{R_s}{R}\right) + \frac{M}{m}kT$$

CME mass is estimated from the white-light images, where enhanced brightness is due to Thomson scattering by electrons (Vourlidas et al. 2000, 2006), ranging from 10^{13-16} grams.

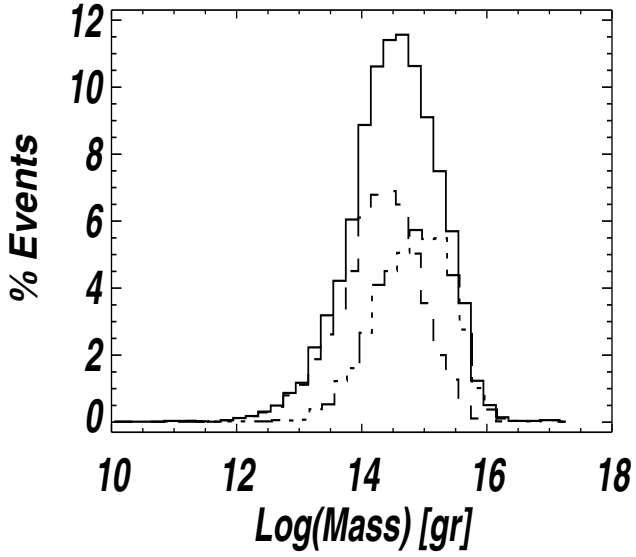

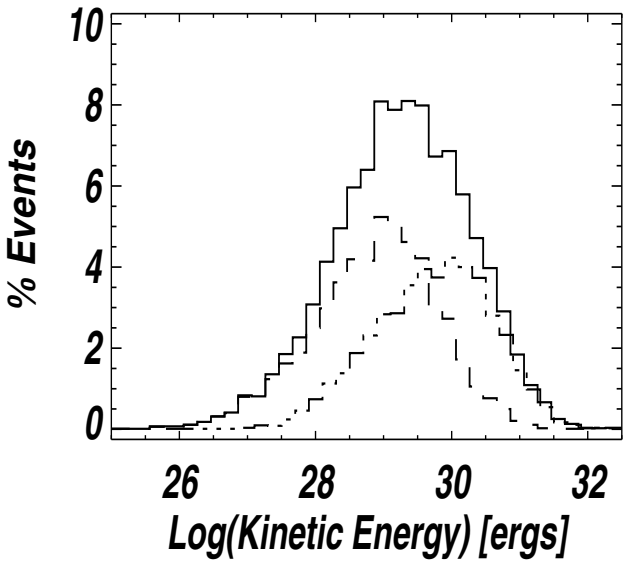

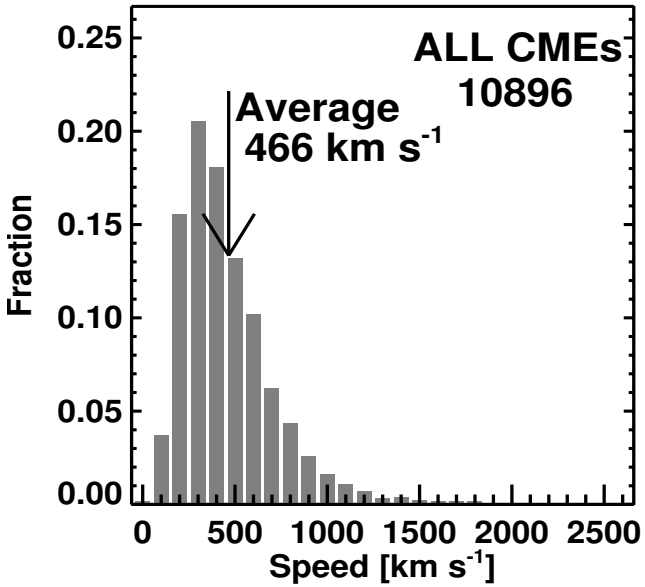

Vourlidas et al.

Gopalswamy, Yashiro at al.

height, velocity, and acceleration of CMEs

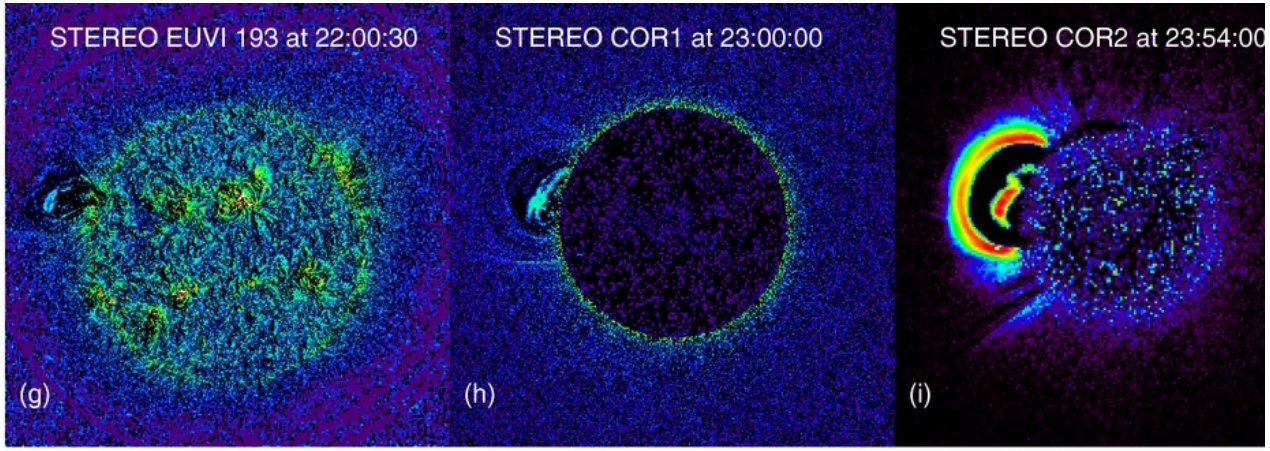

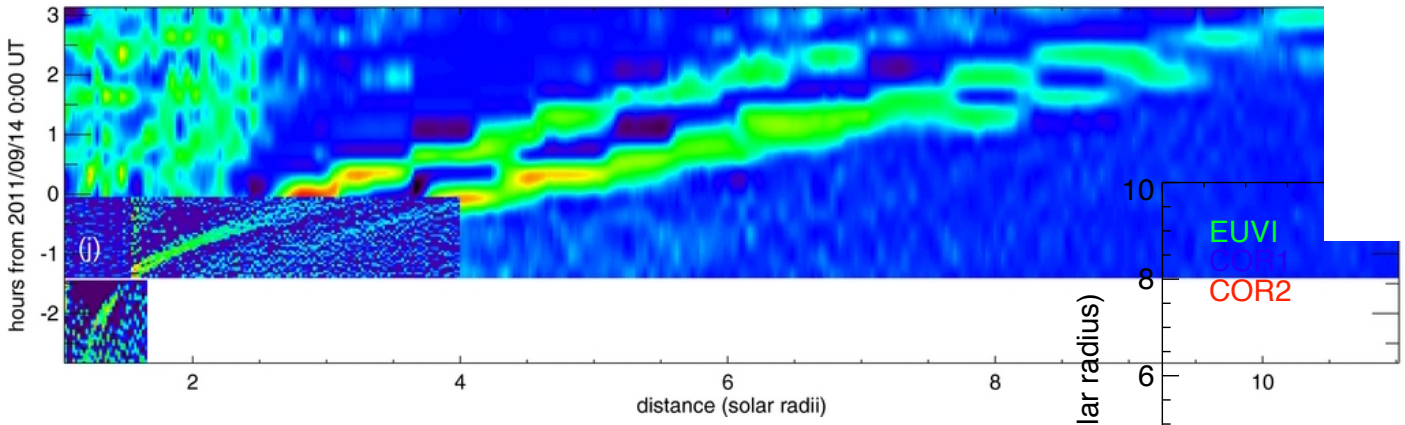

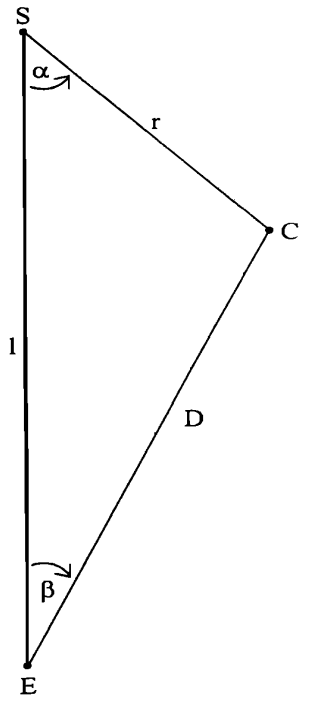

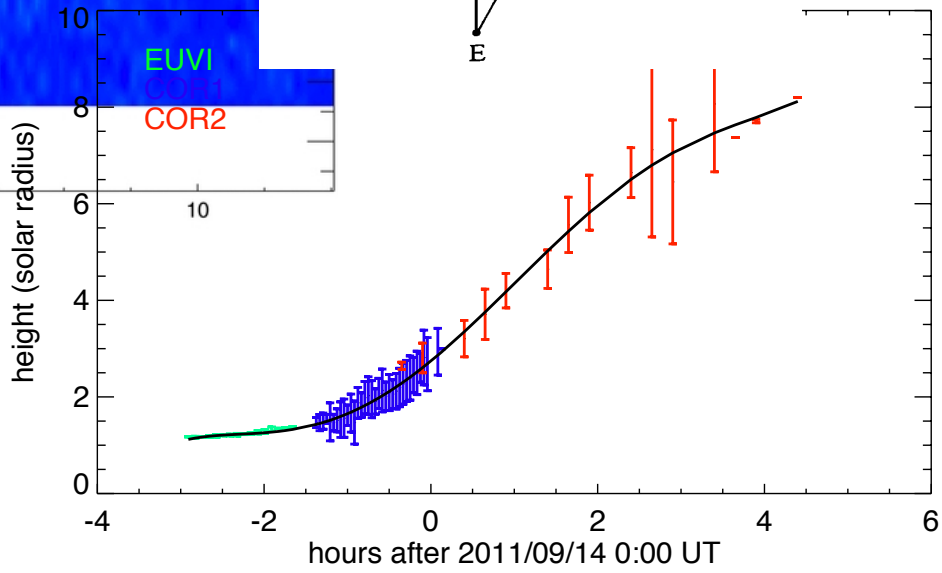

tracking different parts of the CME in a time-height plot, or Jmap (Sheeley et al. 1999).

height, velocity and acceleration of CMEs

Jmap from the twin spacecraft from different views

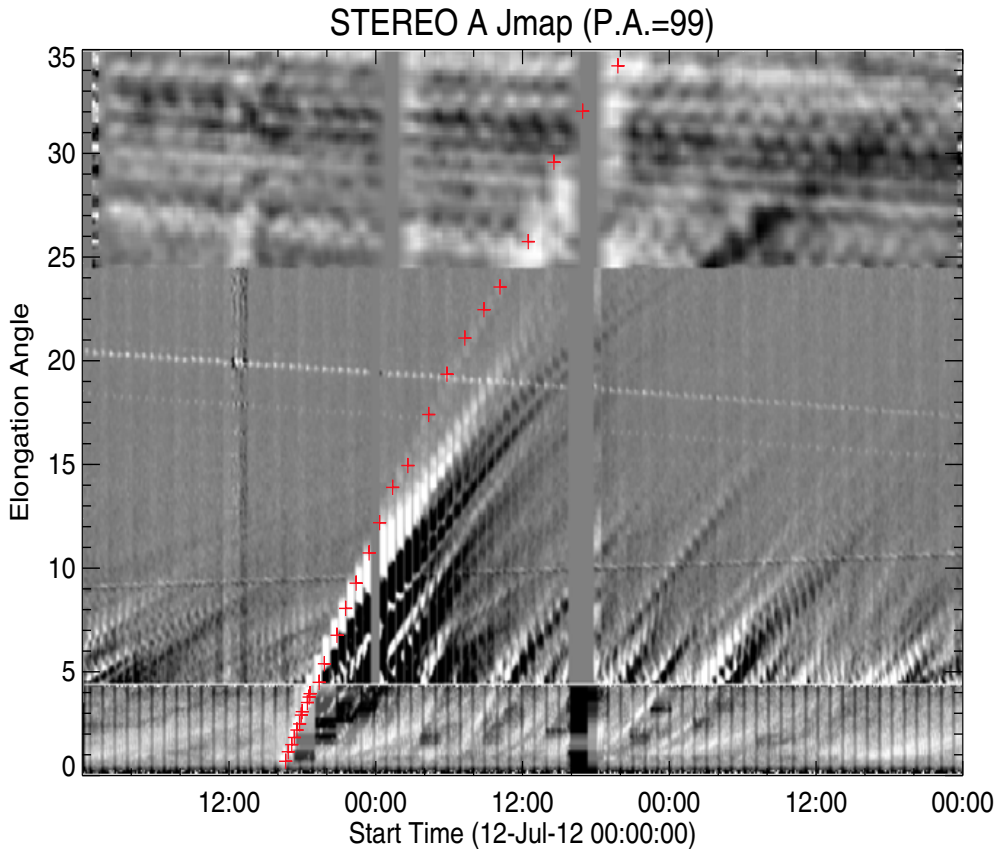

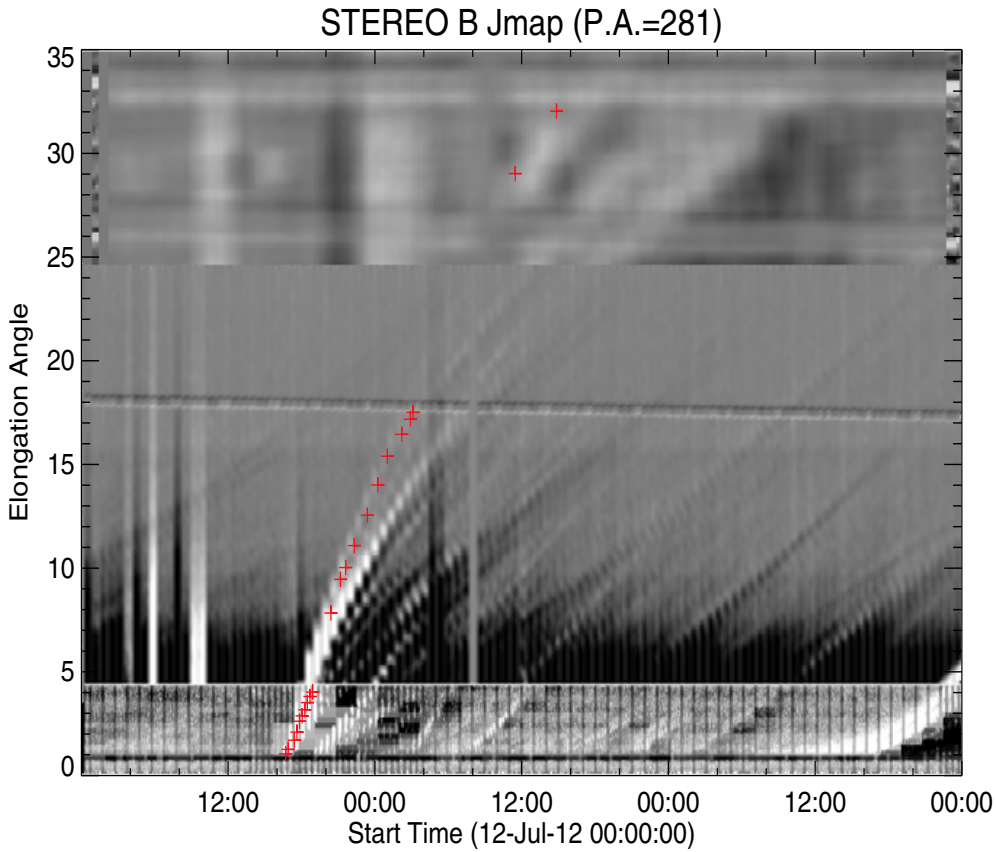

ure 3. Jmaps of the 2012 July 12–14 CME for each *STEREO* spacecraft along the propagation angle as measured by the raytrace method. The CME is cleare

height, velocity and acceleration of CMEs

Forward fitting a CME structure (Thernisien et al. 2006, 2009)

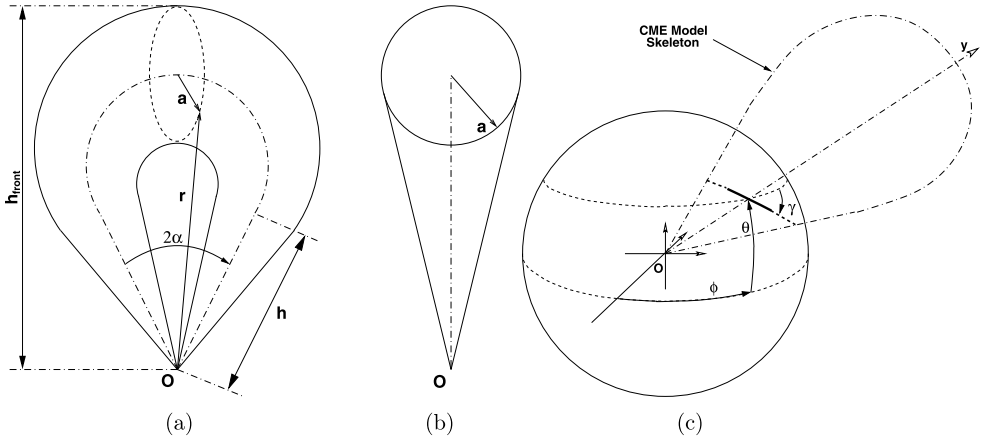

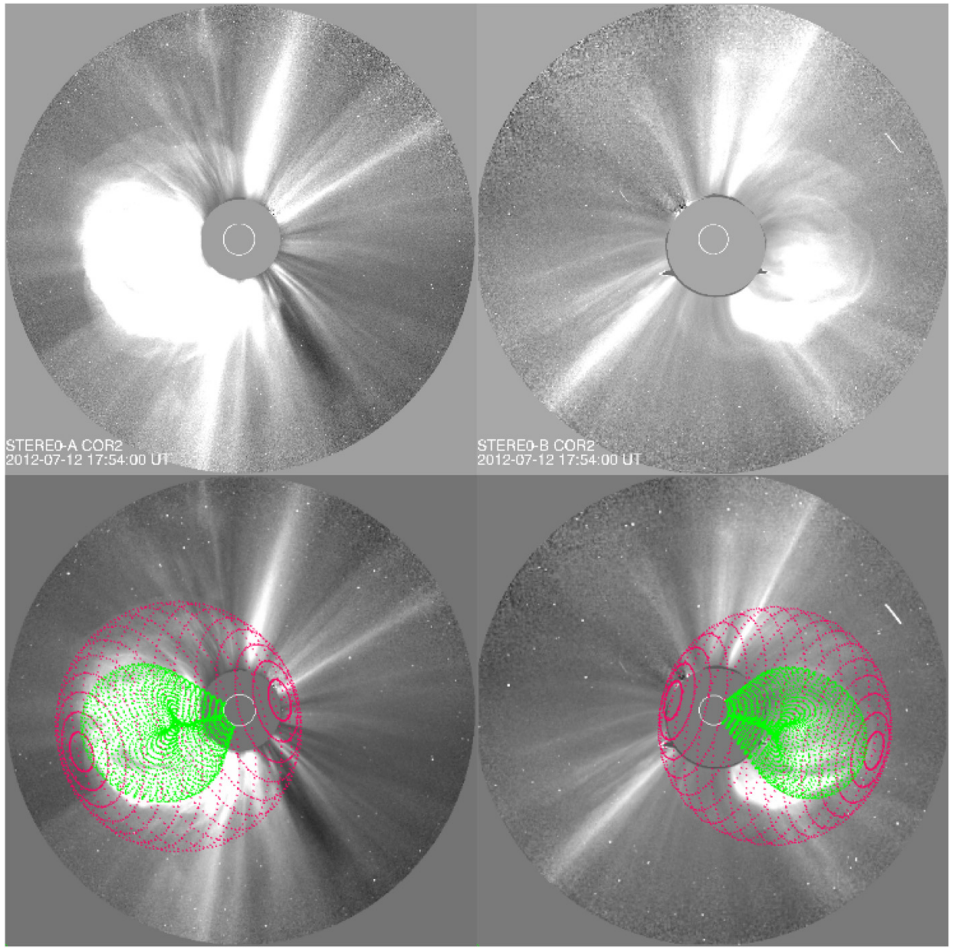

Figure 1. Model fitting of CME ejecta and shock front. Images at 17:54 UT on 2012 July 12 from *STEREO A* COR2 (left) and *STEREO B* COR2 (right) are shown, along without (top) and with (bottom) the raytrace mesh. The green mesh shows the GCS fitting to the CME ejecta, whereas the red mesh shows the spheroid fitting to the CME shock front. A supplemental movie showing the CME and the mesh is provided.

(An animation and a color version of this figure are available in the online journal.)

CME kinematics and flare emissions

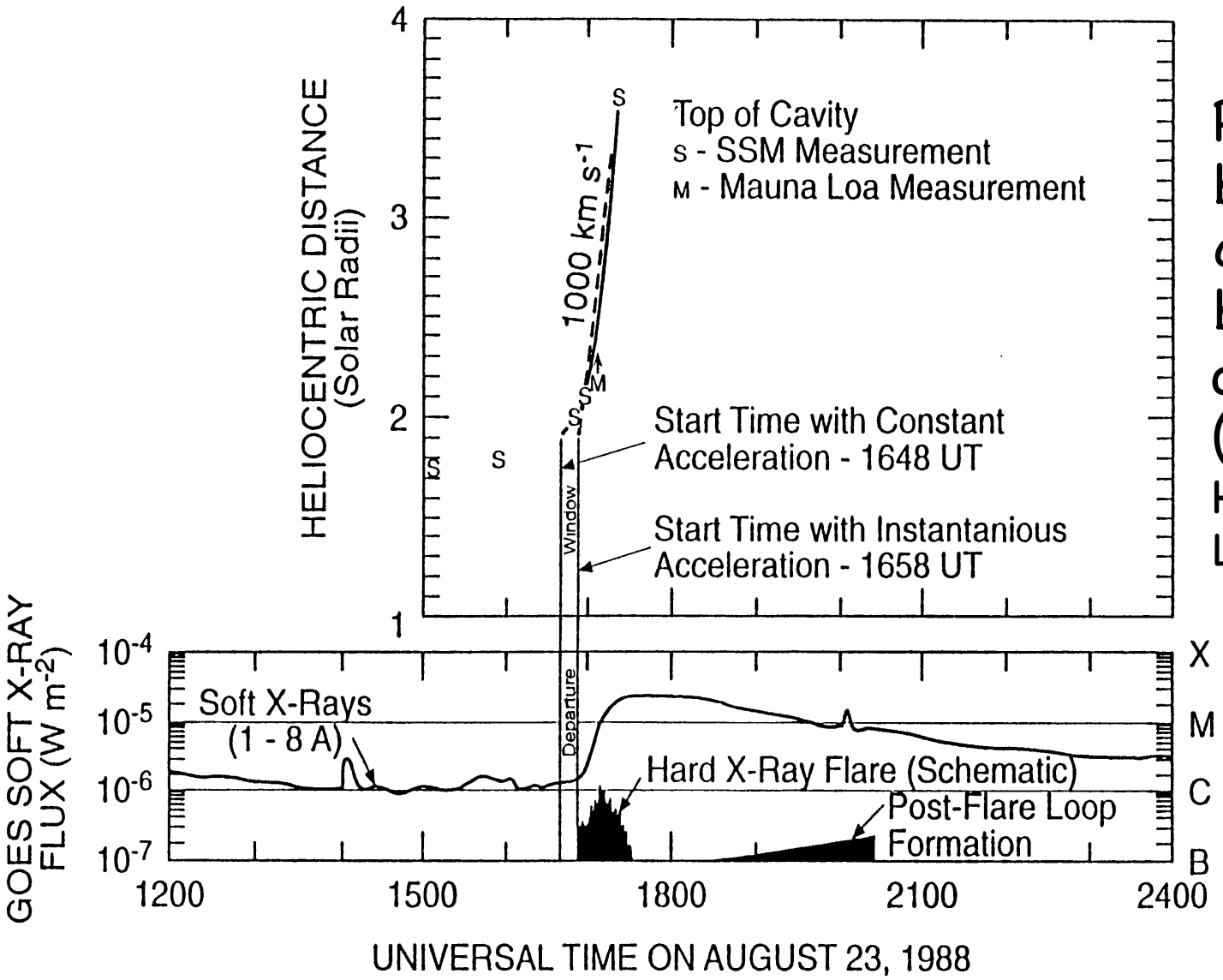

Relationship between flares and CMEs has been studied for decades. (Harrison 1986, Hundhausen 1995, Low 1996)

CME kinematics and flare emissions

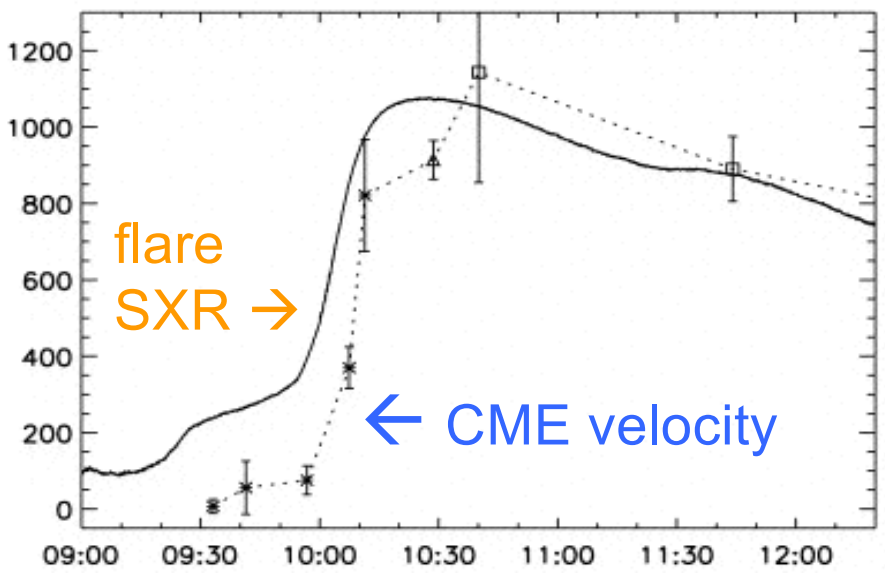

closely related CME motion and flare emission (Zhang et al. 2001; Gallagher et al. 2003 …. Patsourakos et al., 2010 ….)

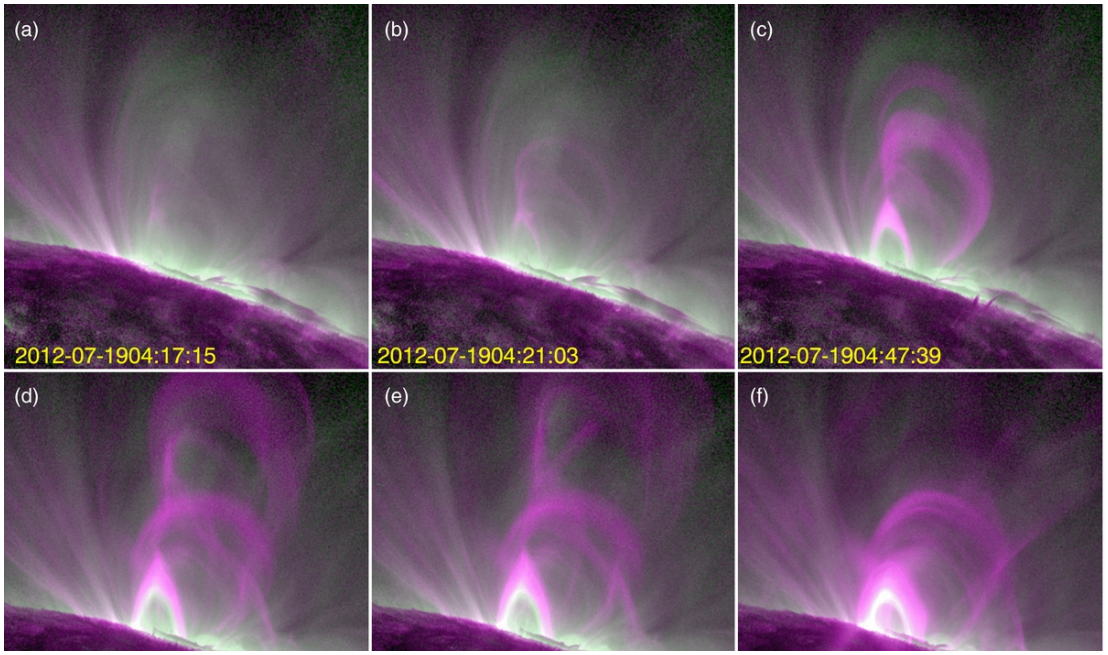

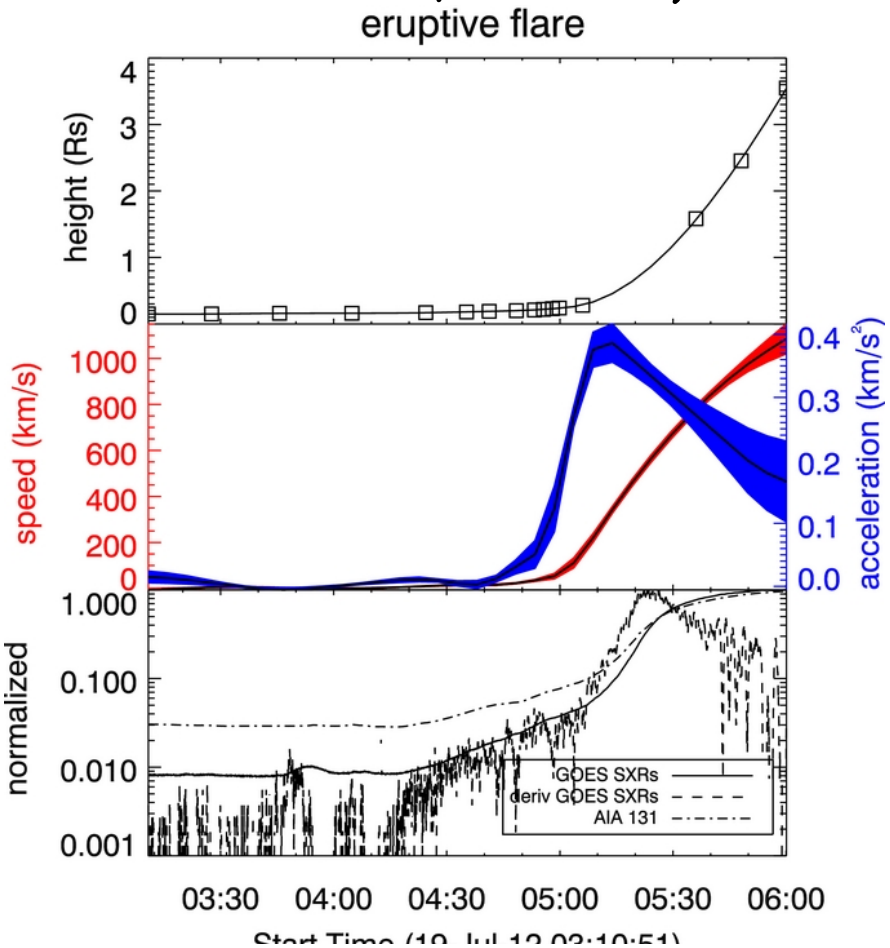

CME kinematics and flare emissions

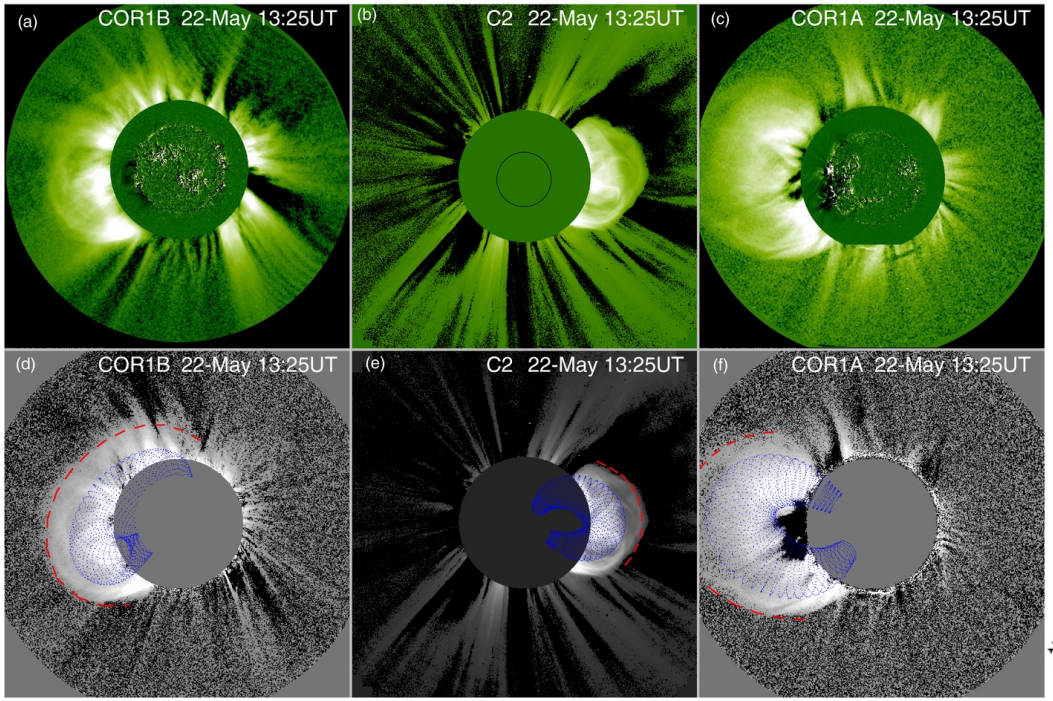

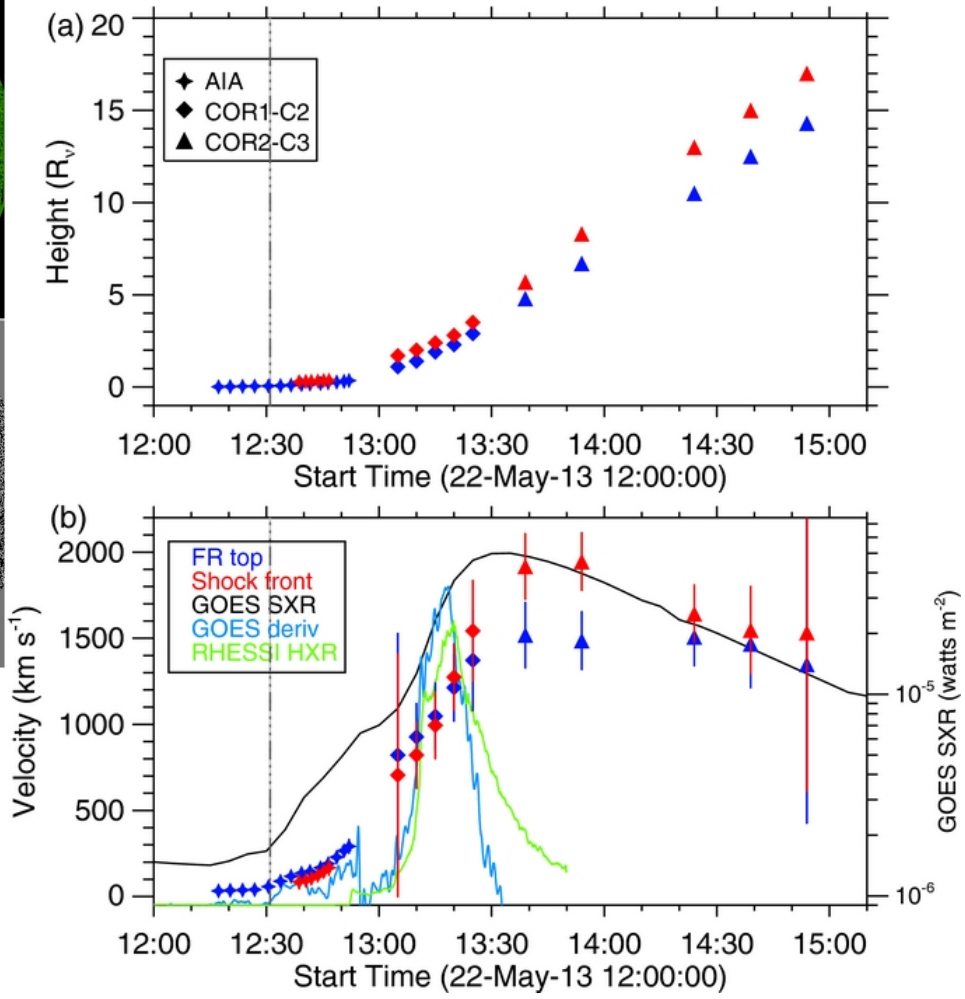

Acceleration of many CMEs takes place early in their life, during the rise phase of flare emission.

Cheng et al. 2014 ……

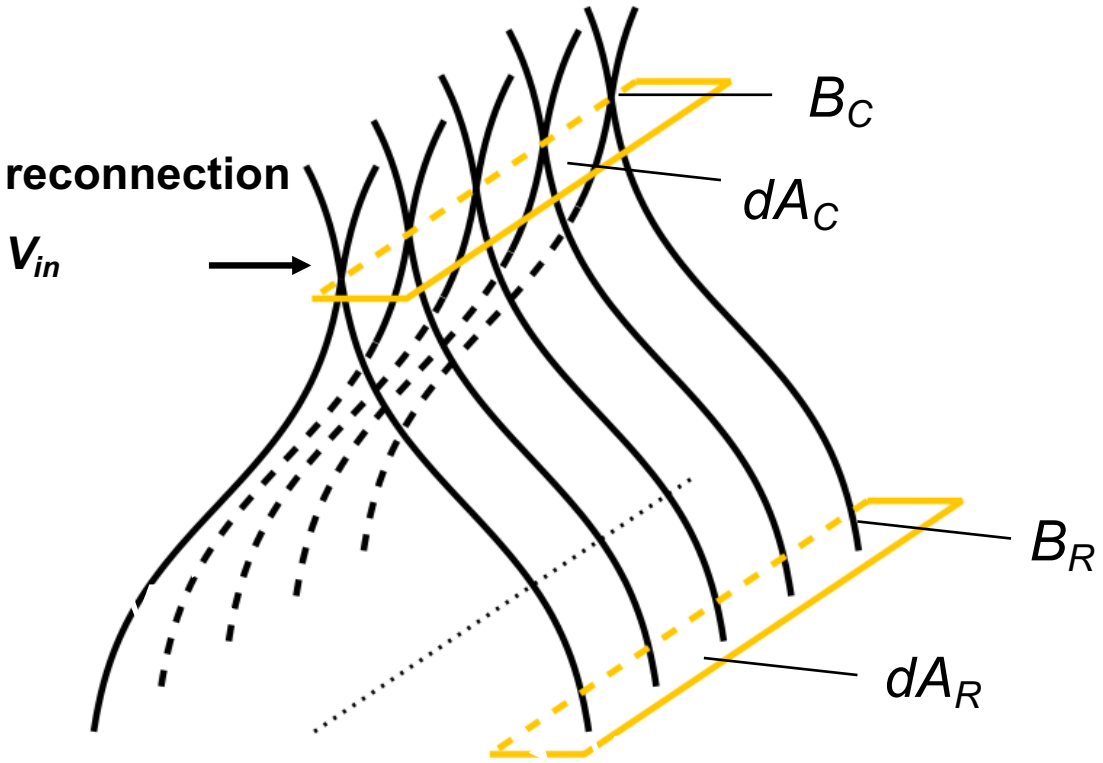

Model: Forbes & Priest

Observation: Poletto & Kopp 1986, Fletcher et al. 2001, 2004, Qiu et al. 2002-2012, Isobe et al. 2002, 2005, Asai et al. 2002, 2004, …

$$\Phi = \int B_R dA_R$$

$$E = v_{in} B_{in} = v_R B_R$$

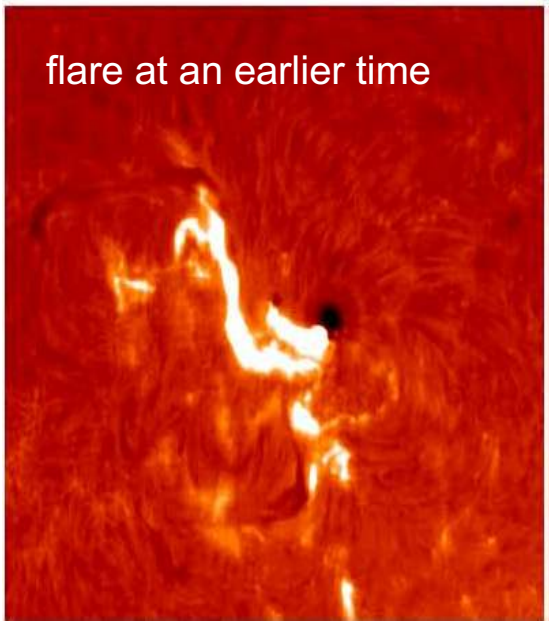

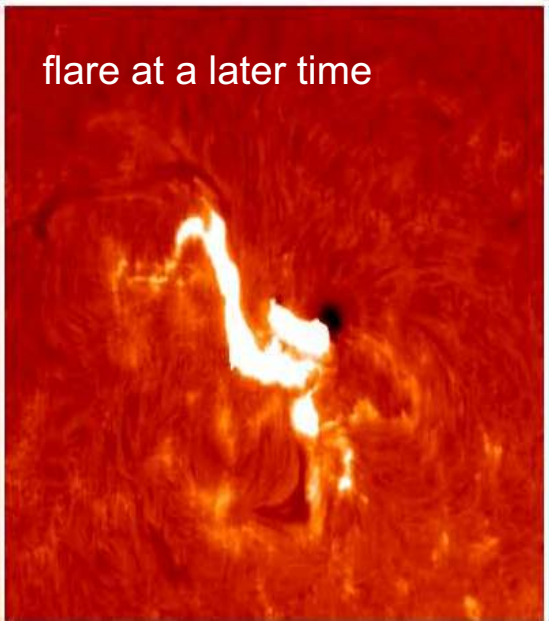

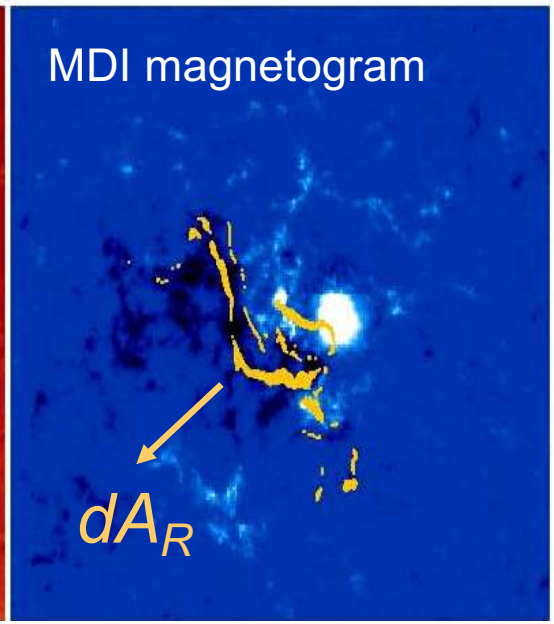

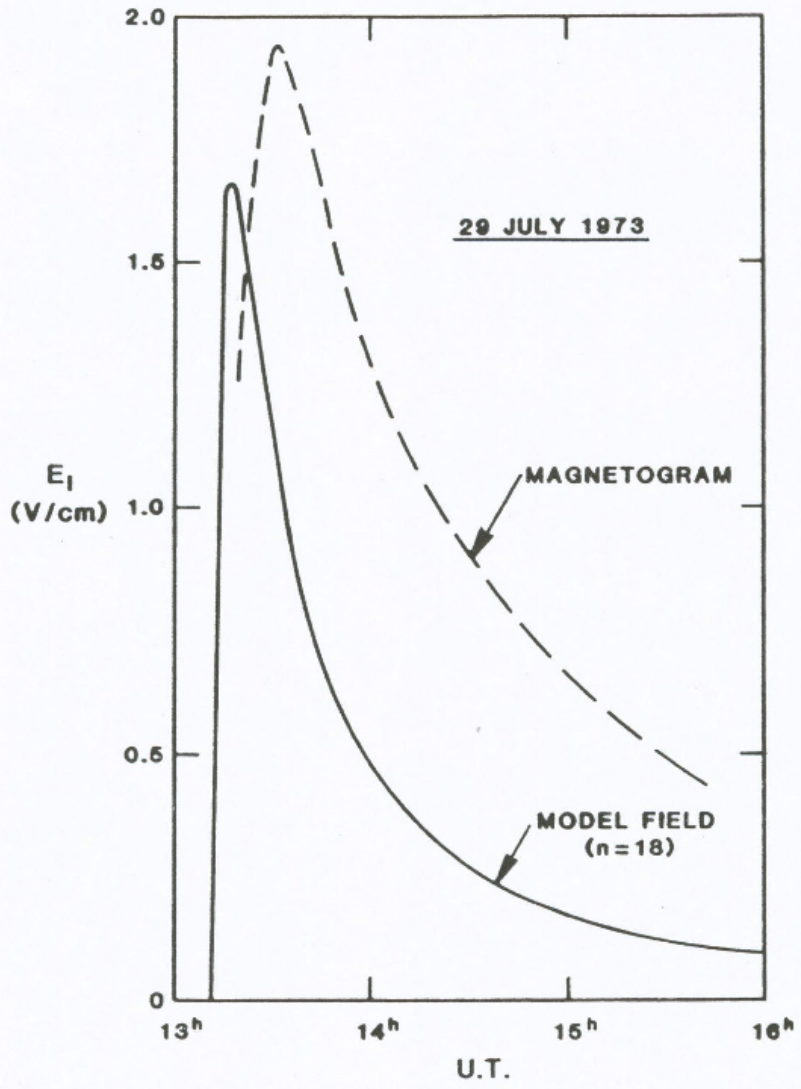

$M_A \sim 0.1$

Measurement of reconnection rate by Poletto and Kopp (1989)

Figure 1. Time history of the neutral-line electric field during the two-ribbon flare of 29 July, 1973, as computed from the Kopp-Poletto magnetic field model (solid curve) and from the method of Forbes and Priest (dashed curve).

CME kinematics and magnetic reconnection

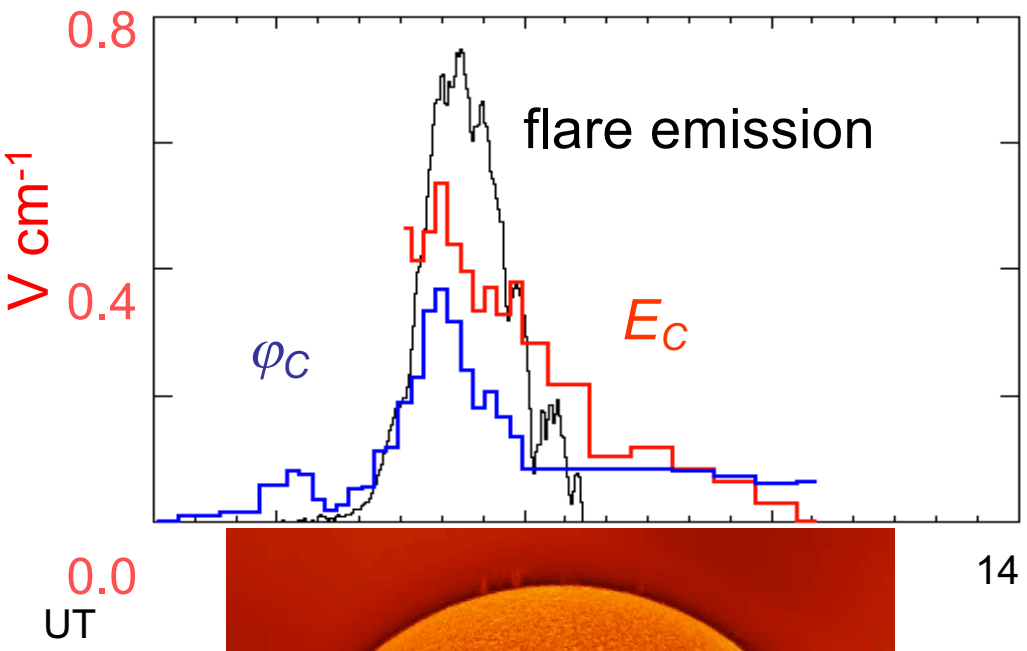

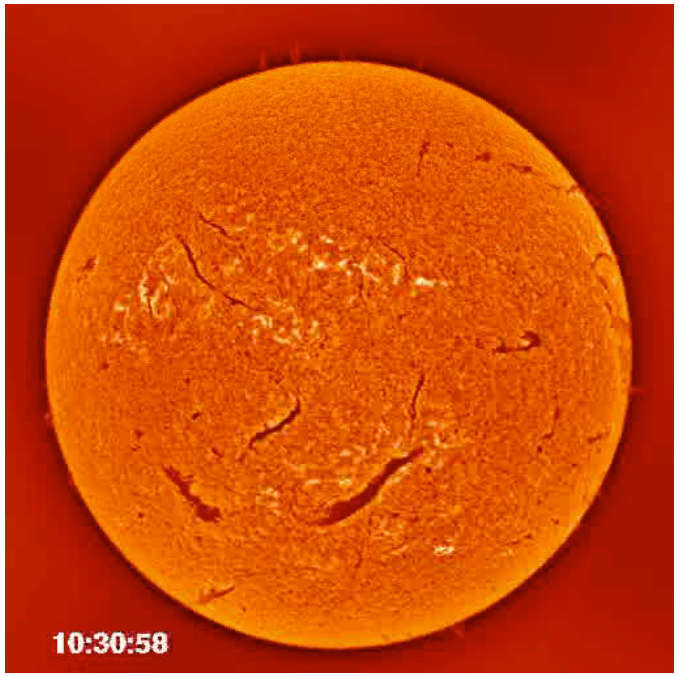

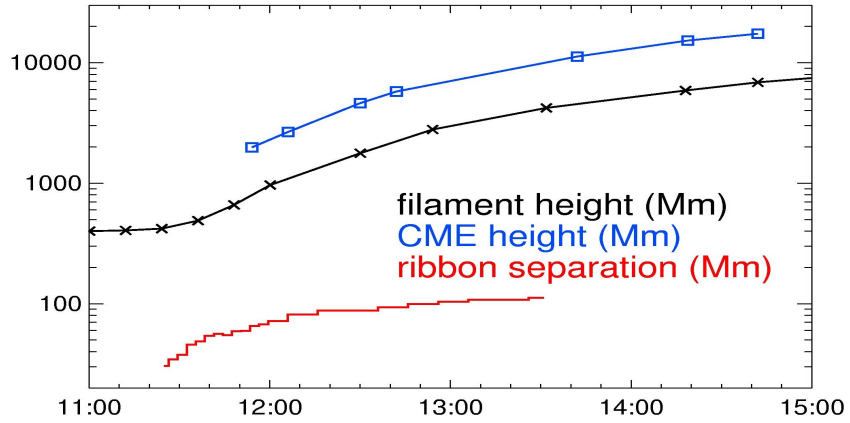

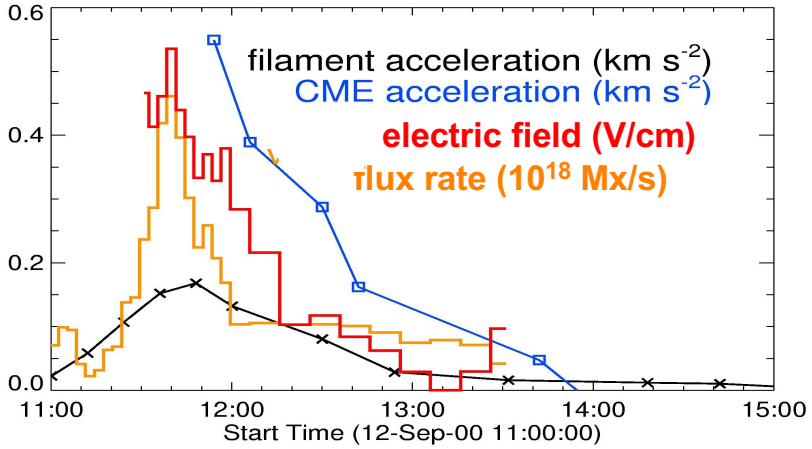

CME evolution often tracks reconnection rate measured in flares (Qiu et al. 2004-)

CME kinematics and magnetic reconnection

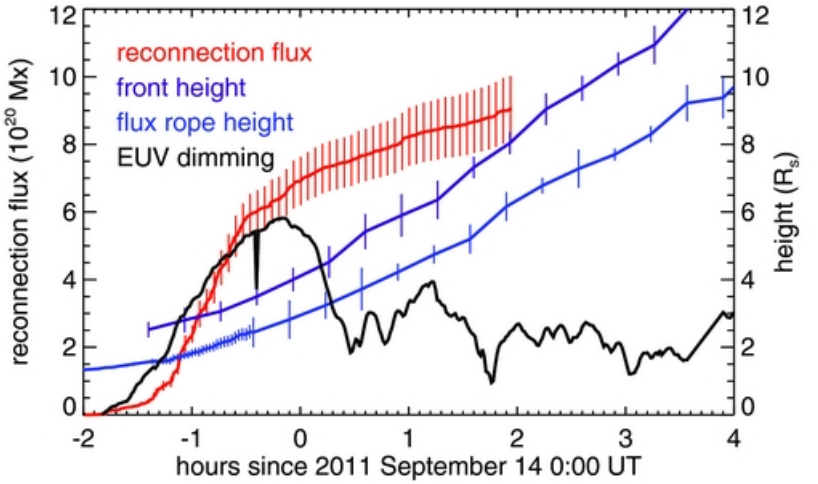

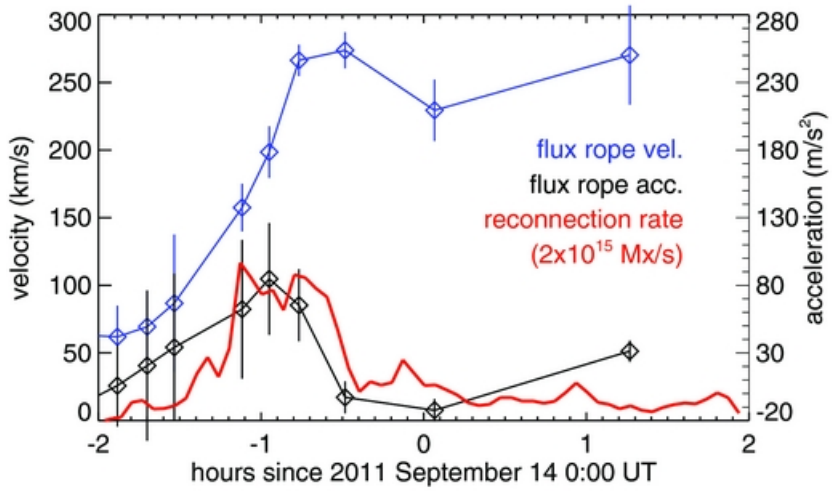

Measurements with instruments from different views.

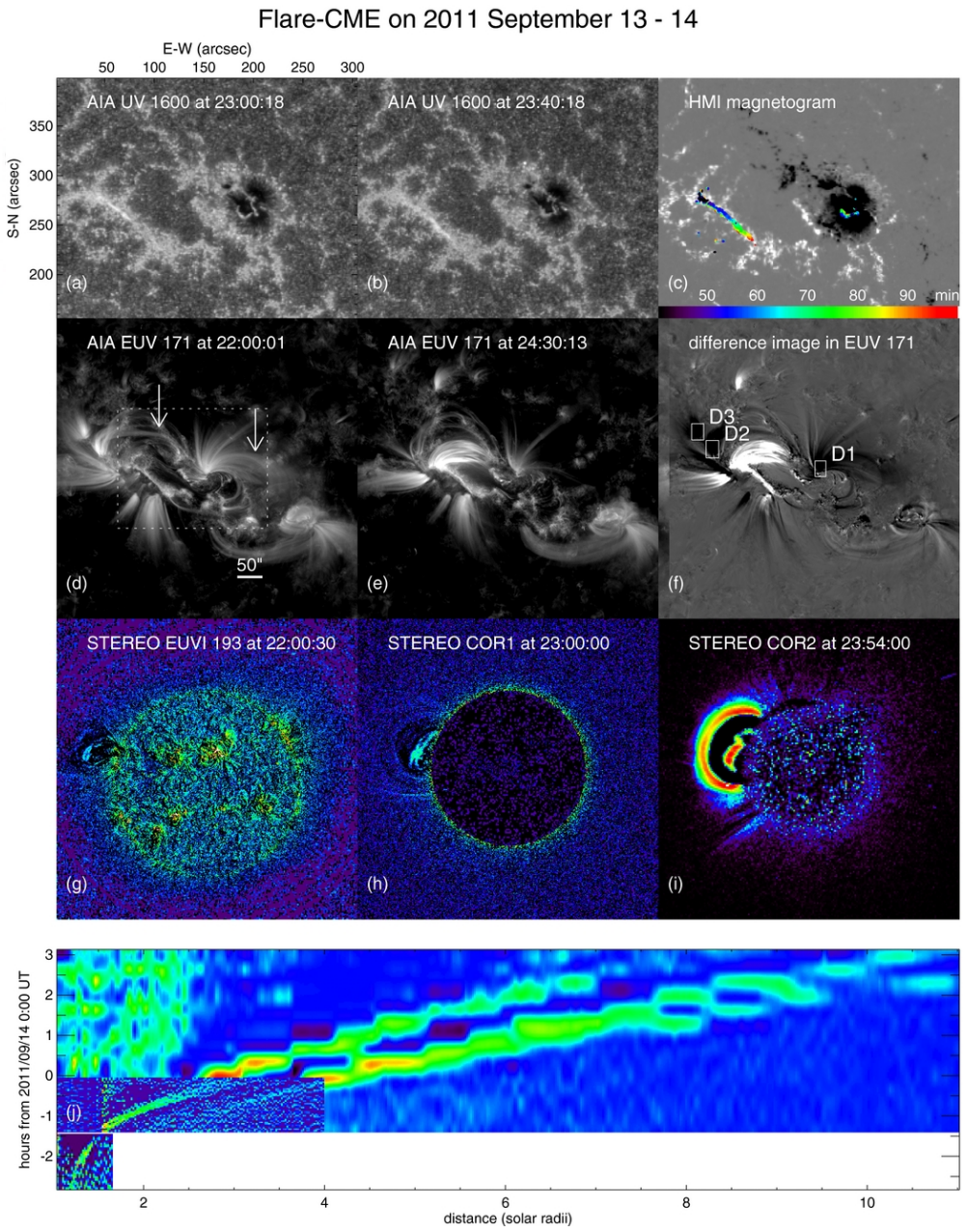

CME kinematics and magnetic reconnection

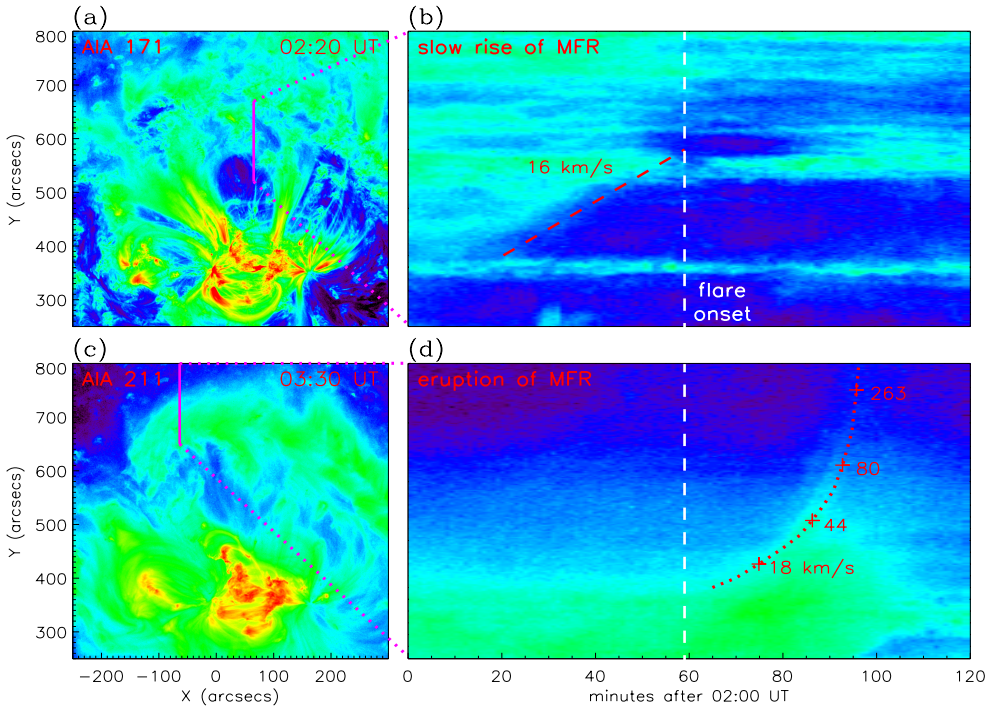

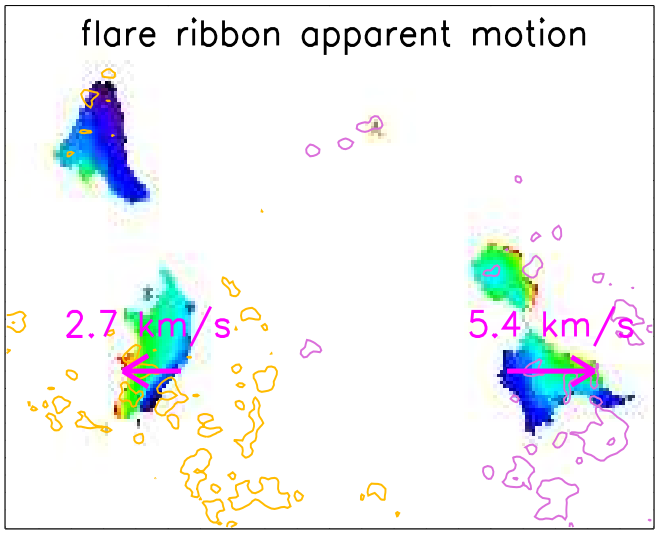

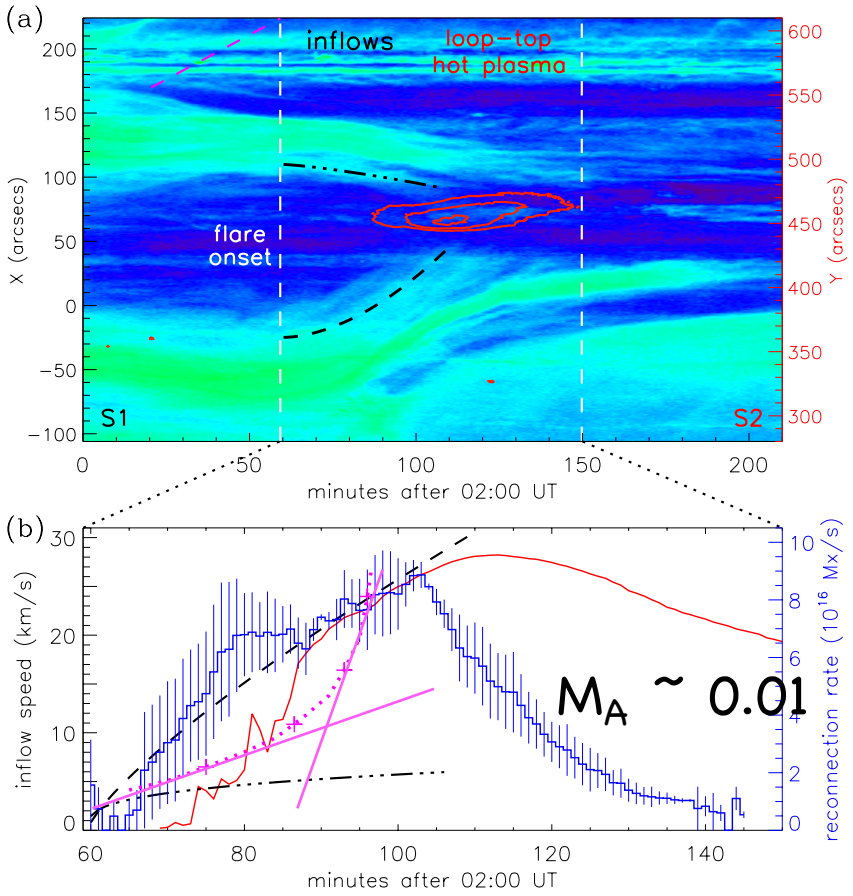

Measure CME and reconnection multiple ways (Li et al. 2017)

CME kinematics and magnetic reconnection

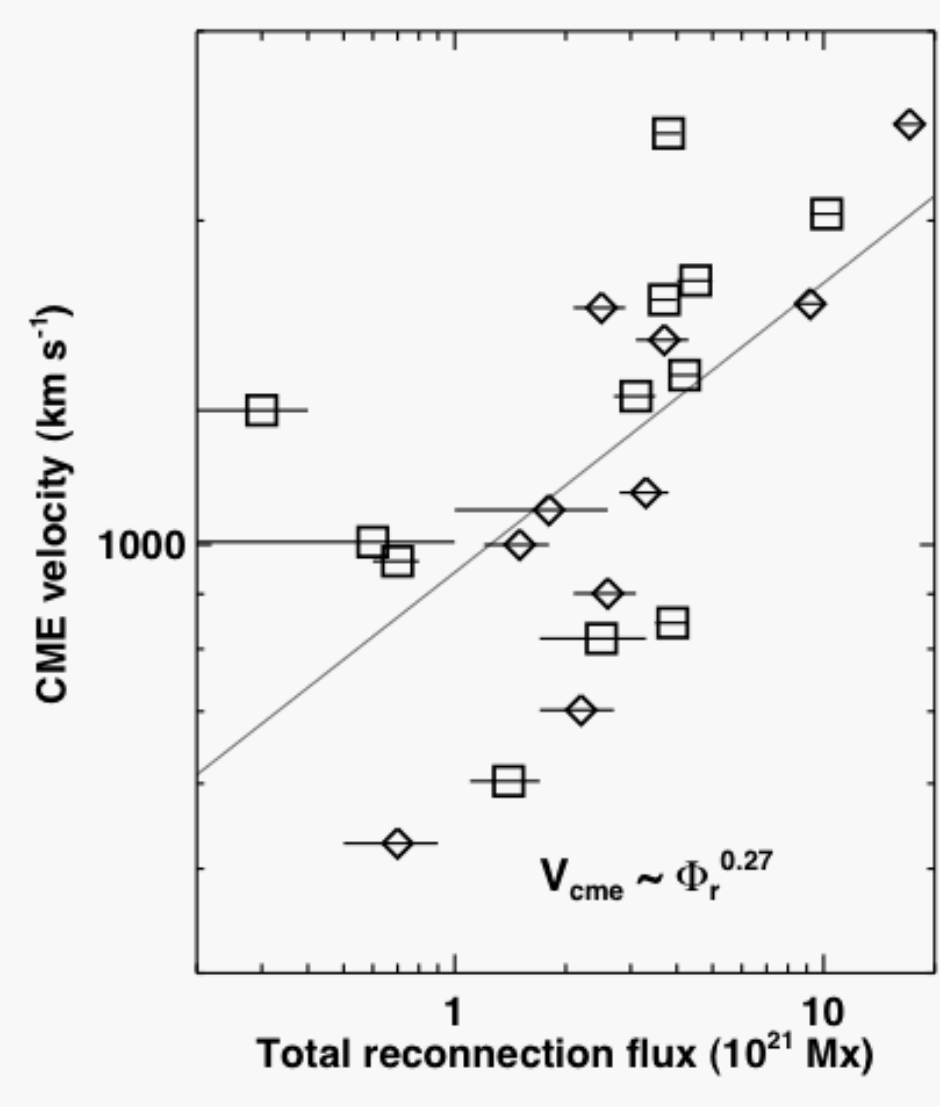

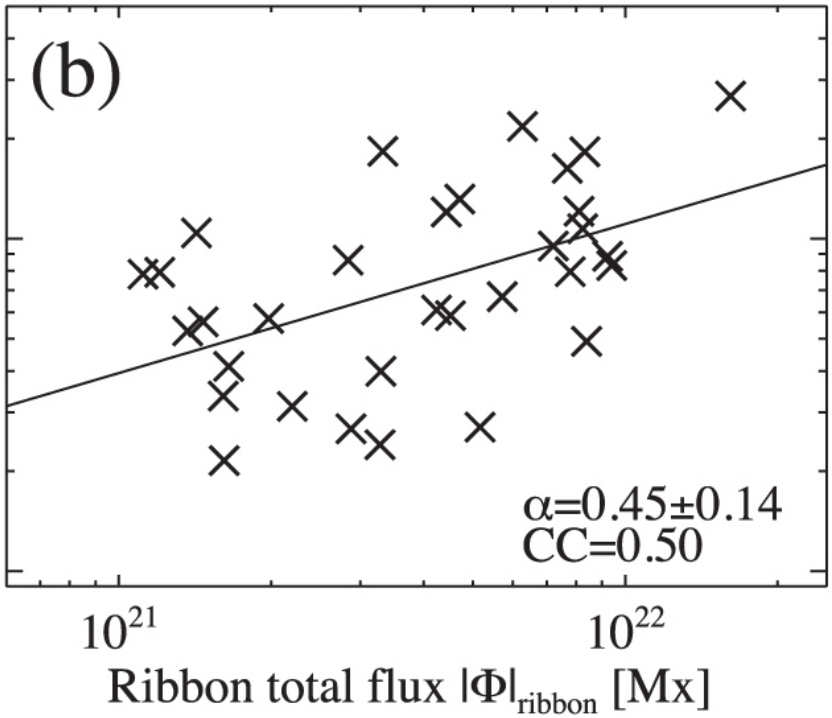

CME speed and reconnection flux (Qiu et al. 2005, Toriumi et al. 2017, Welsch et al. 2017)

model prediction

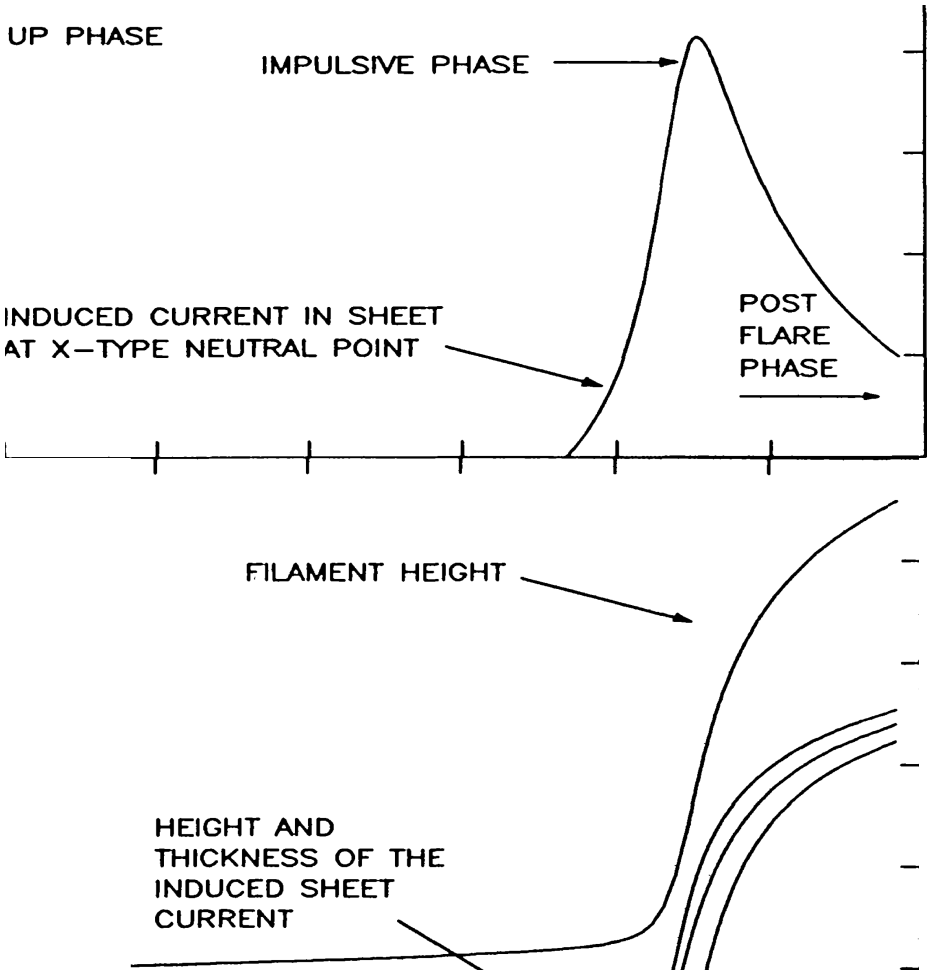

Martens & Kuin 1989

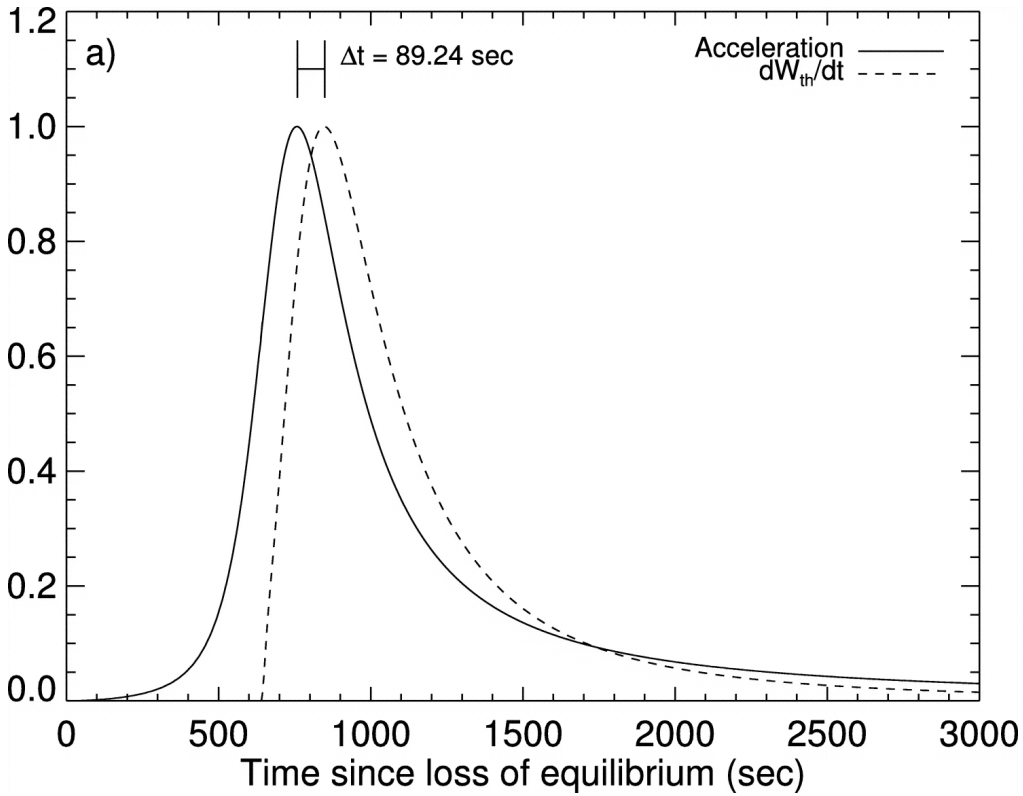

Reeves (2006) (and Forbes-Isenberg-Lin-Reeves)

model prediction

b

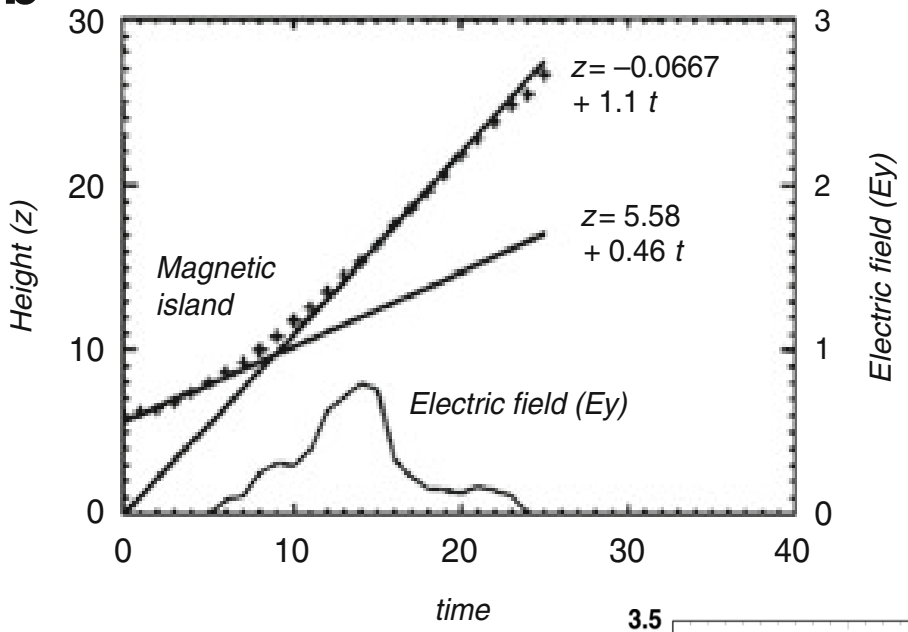

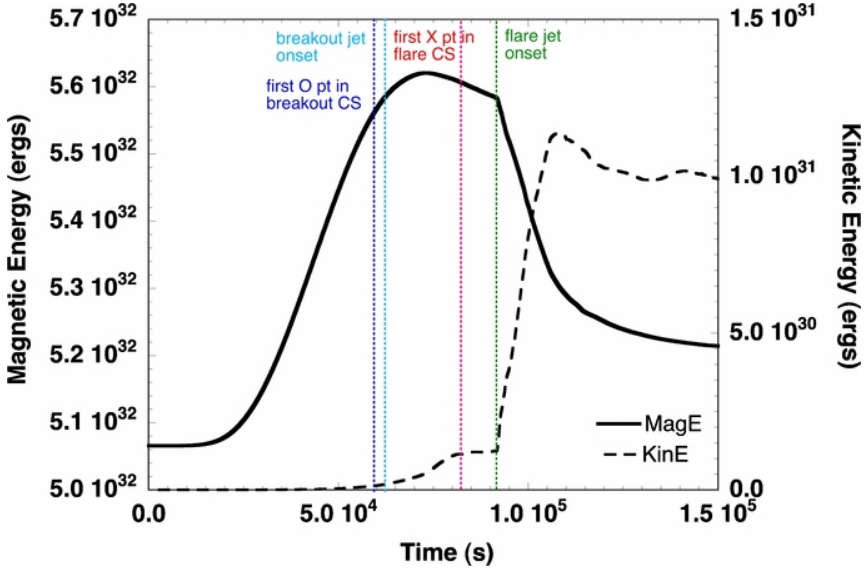

Numerical models indicating timing of reconnection and CME acceleration.

Magara et al. (1997), Shibata et al (2001), Karpen et al. (2012) ….

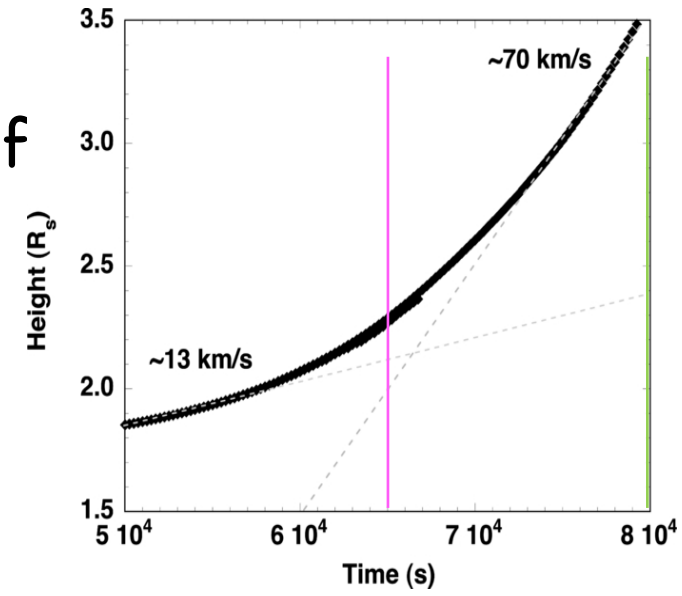

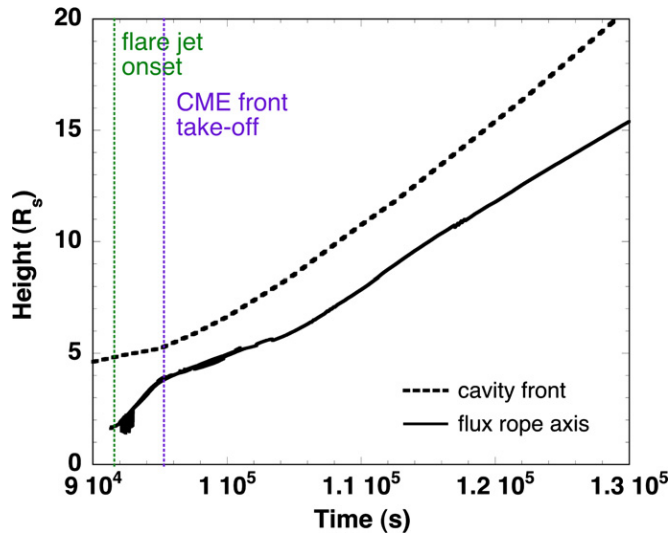

Figure 15. Height of the cavity front and flux-rope axis vs. time. Here the front is defined as the location where the mass density increases sharply behind the breakout current sheet, and the flux-rope axis is an O-type null. A thicker track is shown in certain intervals before ~102,000 s because two O-type nulls exist

not all eruptions are success

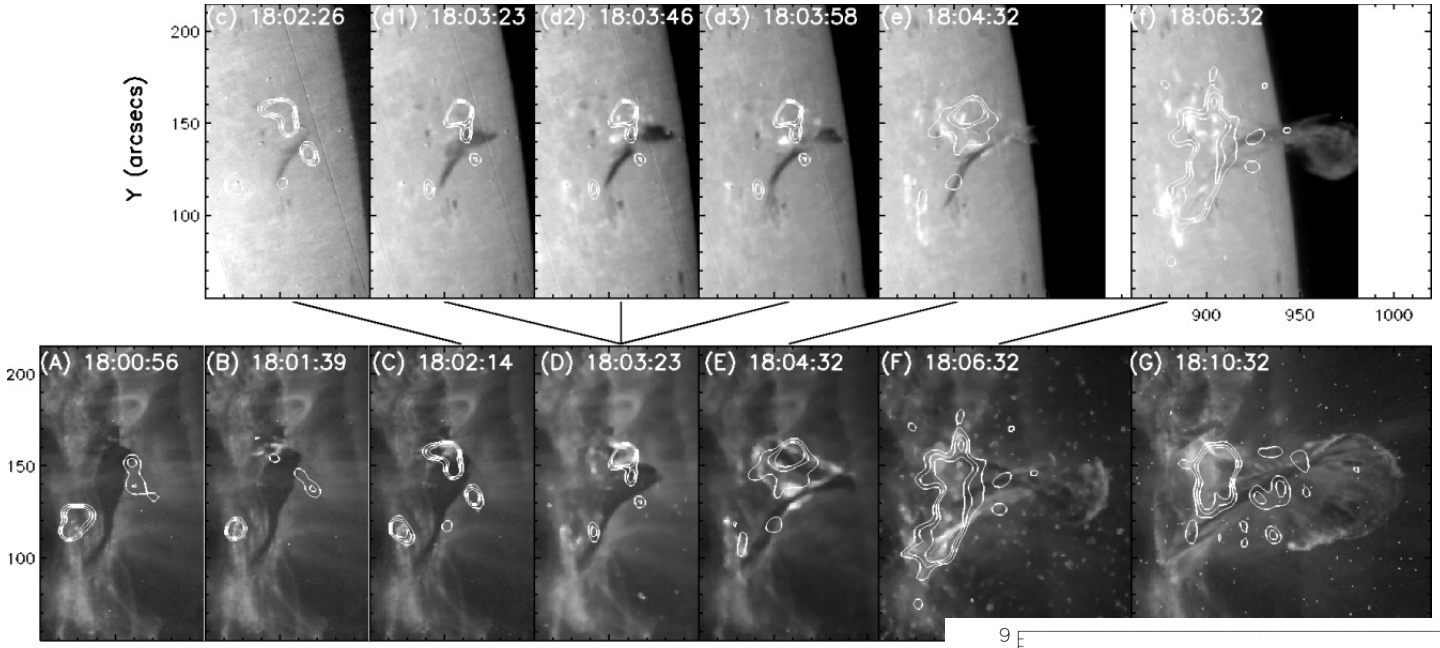

Occasionally, failed filament eruptions are observed (Ji et al. 2003)

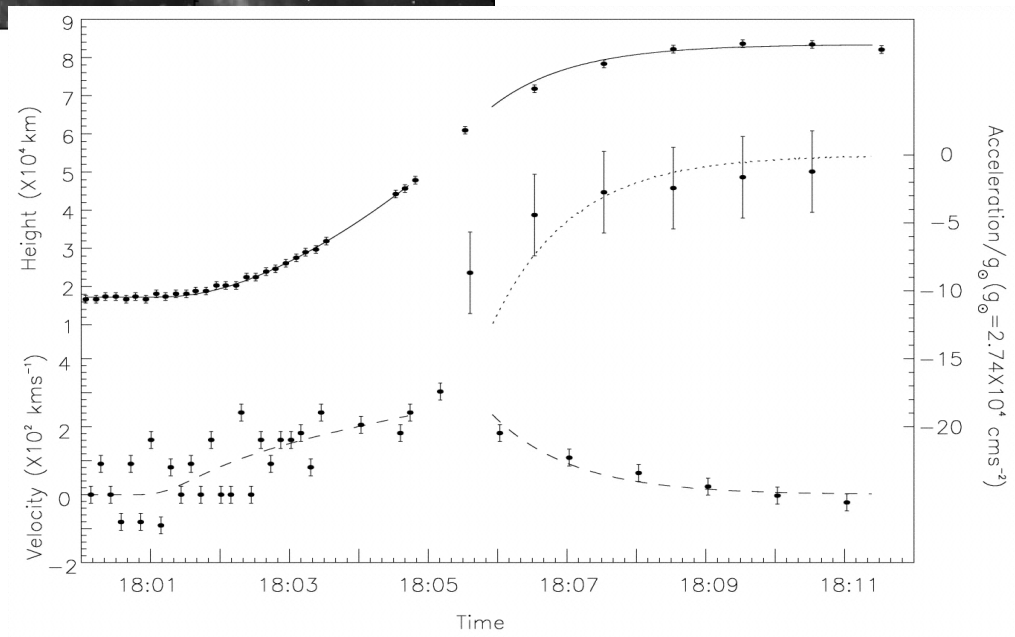

erupt or not, and why

Magnetic properties of primordial CMEs and their surrounding from magnetic field extrapolations, e.g., NLFF, PFSS, used to test instability models (Liu et al. 2008 ...)

TABLE 2

THREE TYPES OF ERUPTION: AVERAGE

Type	Flux (e22) (Max)	n_1 (NL)	B_{t1} (NL) (G)	n_2 (AR)	B_{t2} (AR) (G)
FE	6.60 ± 0.33	1.62 ± 0.05	63.3 ± 18.0	1.42 ± 0.13	36.4 ± 11.8
KI	2.16 ± 1.25	1.93 ± 0.15	22.3 ± 9.8	1.72 ± 0.19	13.7 ± 6.5
TI	4.13 ± 0.43	1.89 ± 0.15	29.7 ± 3.3	1.57 ± 0.15	14.8 ± 3.2
KI+TI	2.81 ± 1.48	1.91 ± 0.15	24.7 ± 8.2	1.67 ± 0.18	14.0 ± 5.4

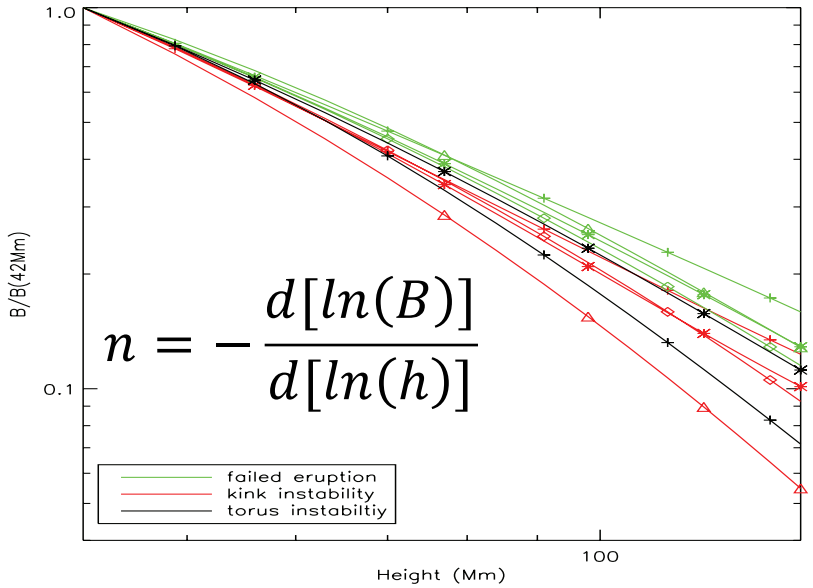

FIG. 2.—Profile of horizontal magnetic field above the erupted regions. The field is averaged along the magnetic neutral line of the active region where the eruption took place. This is a log-log plot. The green, red, and black curves represent FE, KI, and TI, respectively. The green and red curves with cross, star, diamond, and triangle symbols represent events 1–4 and events 5–8, while

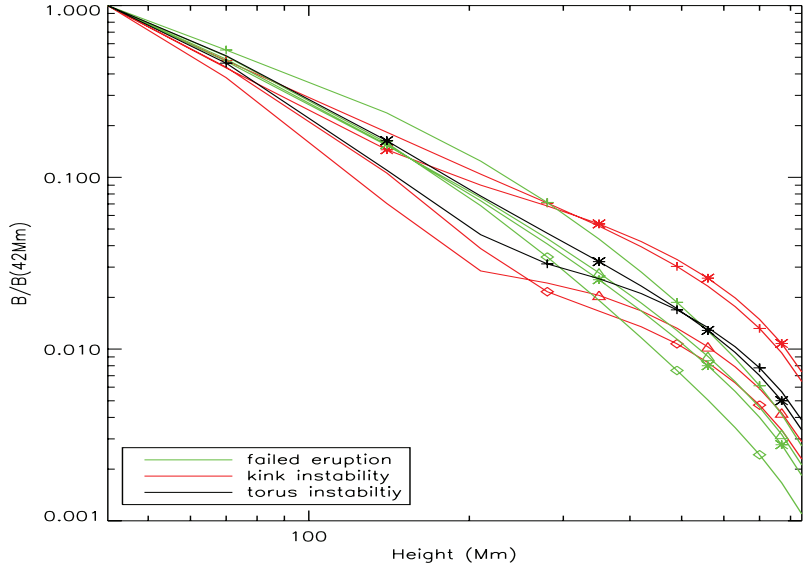

FIG. 3.—Horizontal magnetic field above the erupted regions as a function of height. The field strength and height are both in log units. The height ranges from 42 to 840 Mm. The strength is computed by averaging the whole area of the active region where the eruption took place. Since we are going to examine behaviors of a magnetic field at high altitude that is comparable with the size of active region, the field averaged over the whole active region is

coronal dimming and CME properties

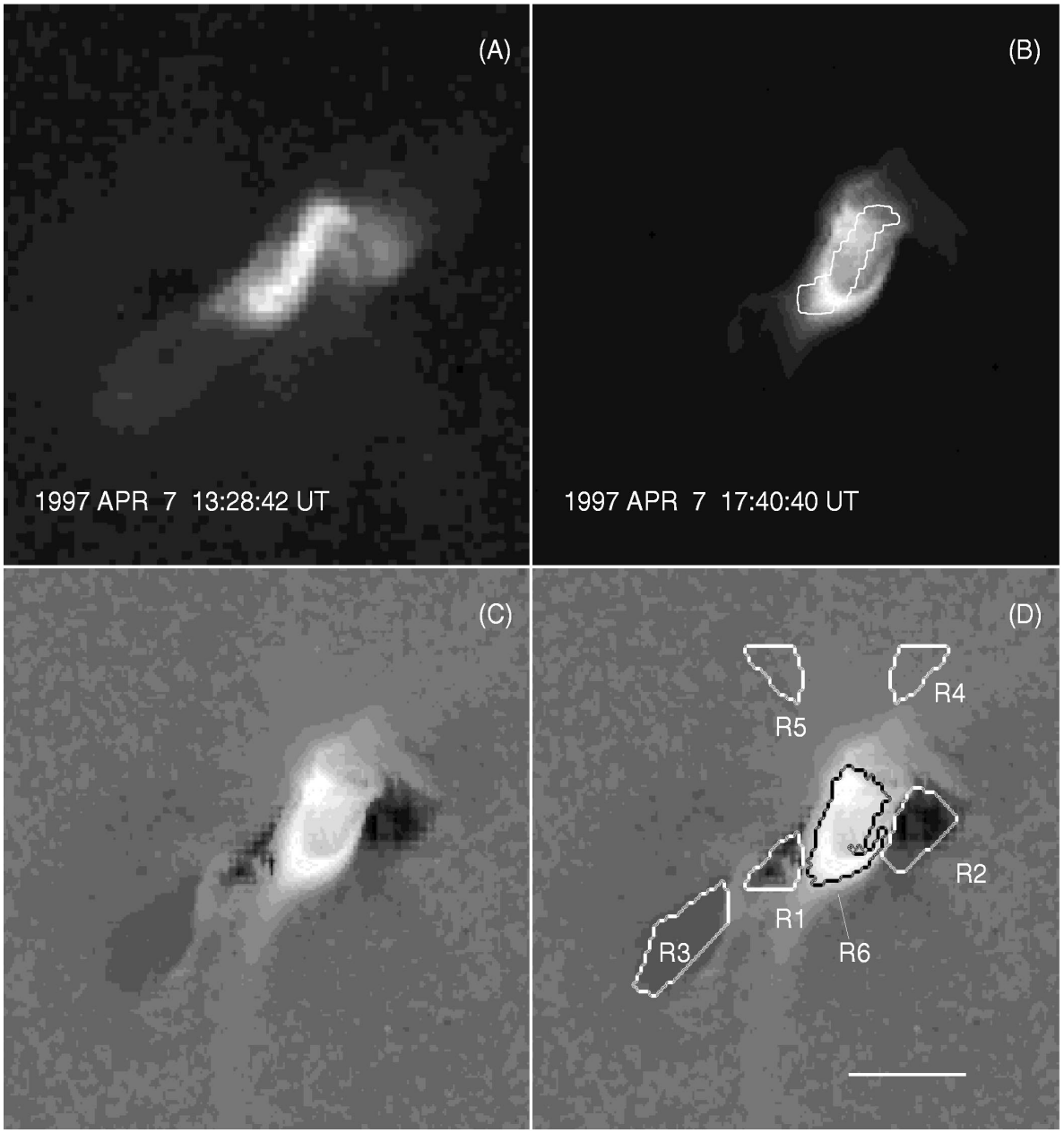

Coronal dimming observed in SXR and EUV images indicates mass "loss" with an erupting CME, estimated to be 10^{14}g (Hudson et al. 1996, Sterling & Hudson 1997)

Coronal dimming and CME properties

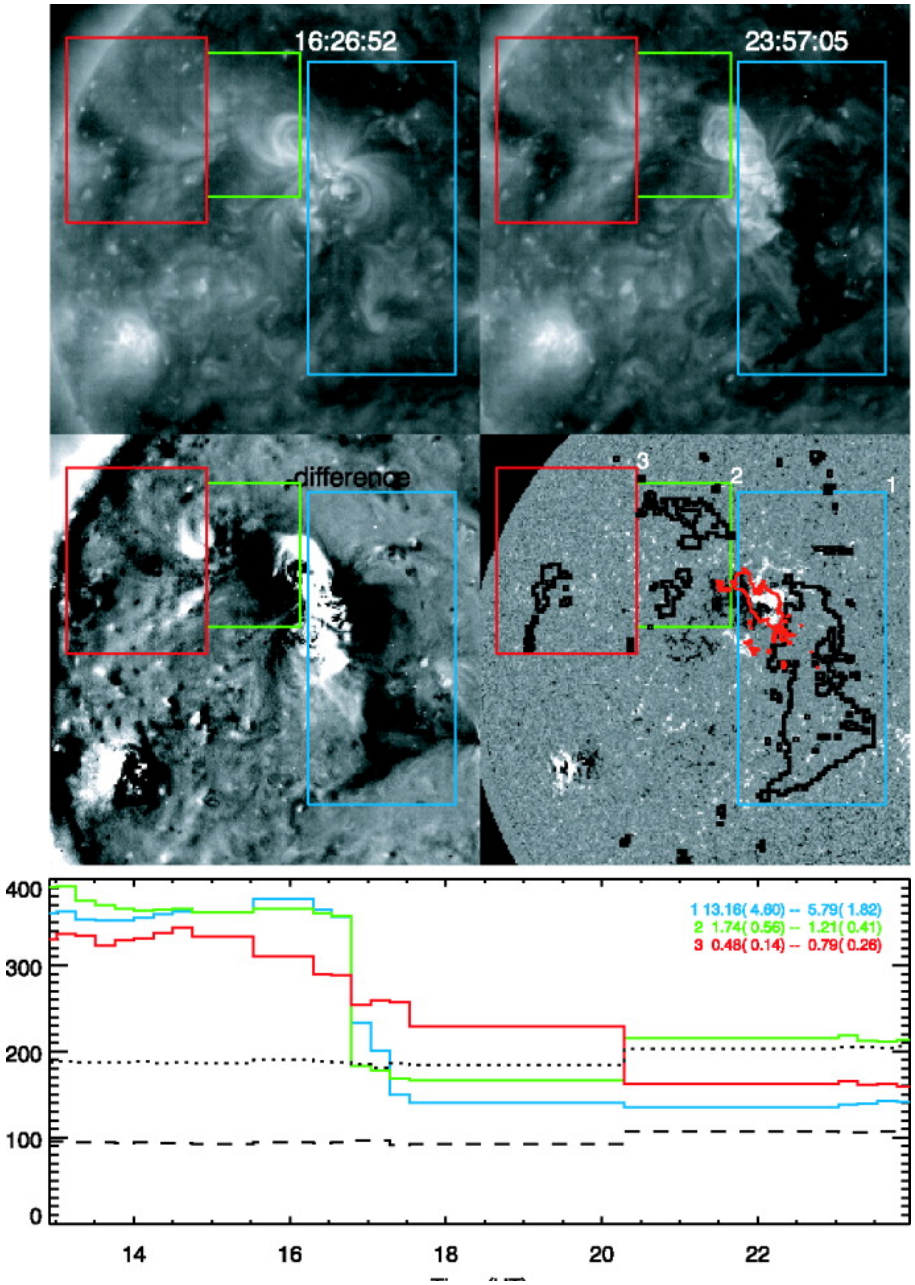

Coronal dimming in EUV images

Coronal dimming and CME properties

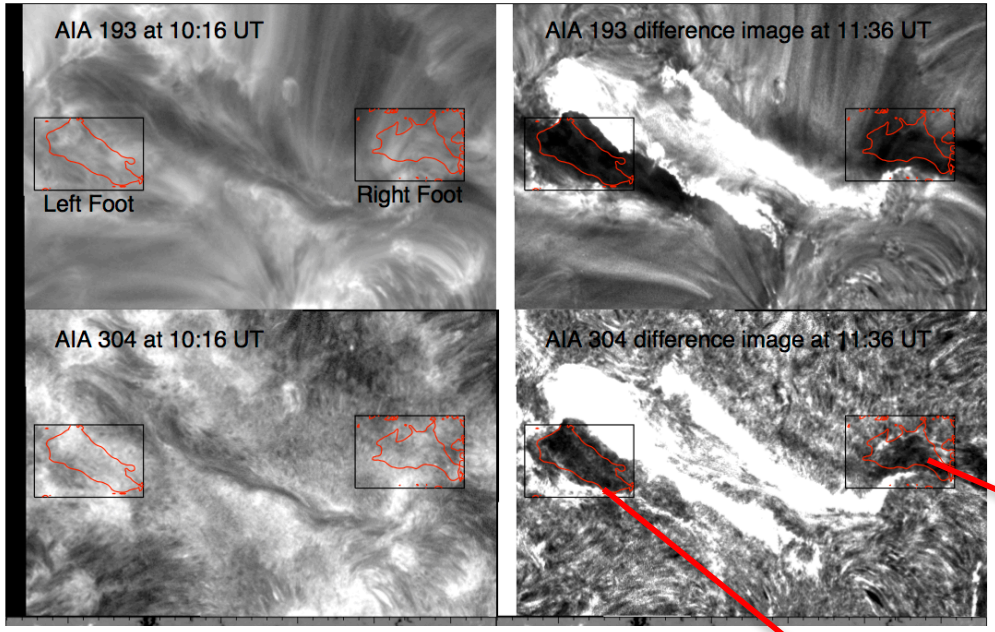

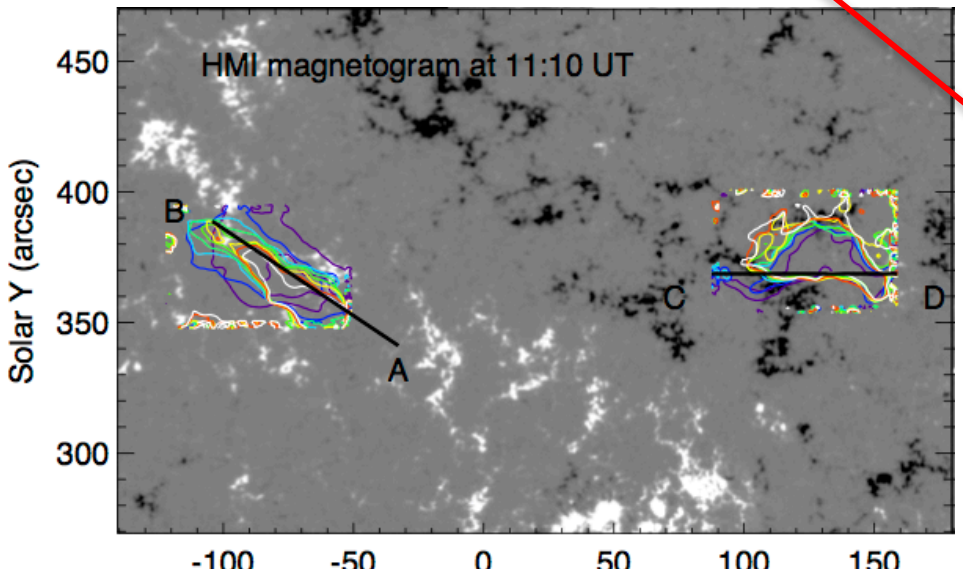

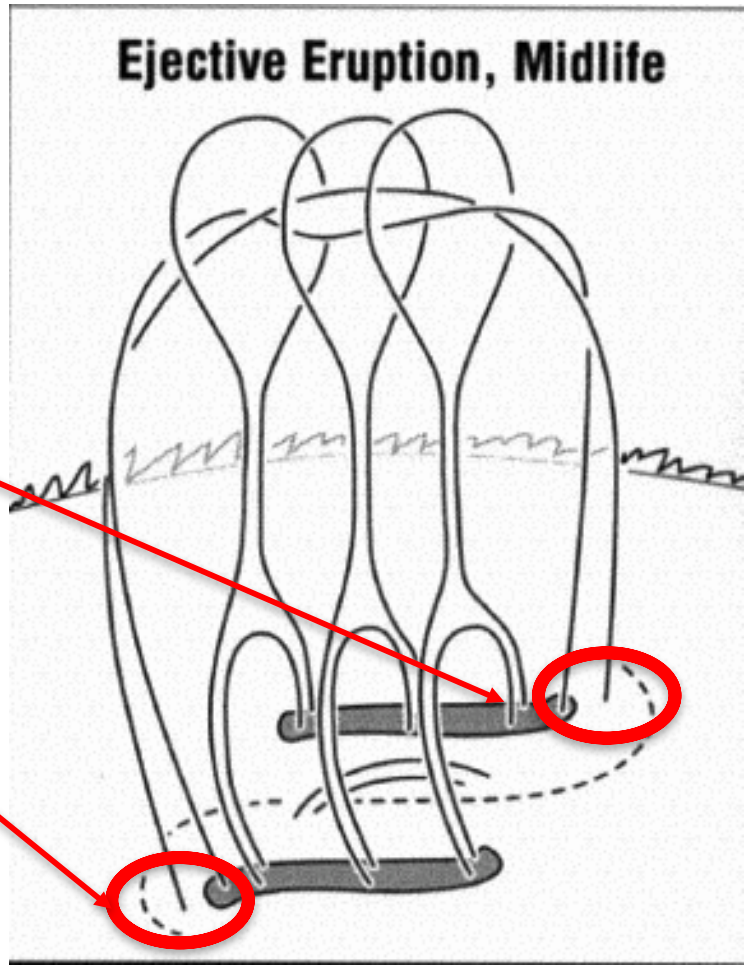

Moore et al. (2001)

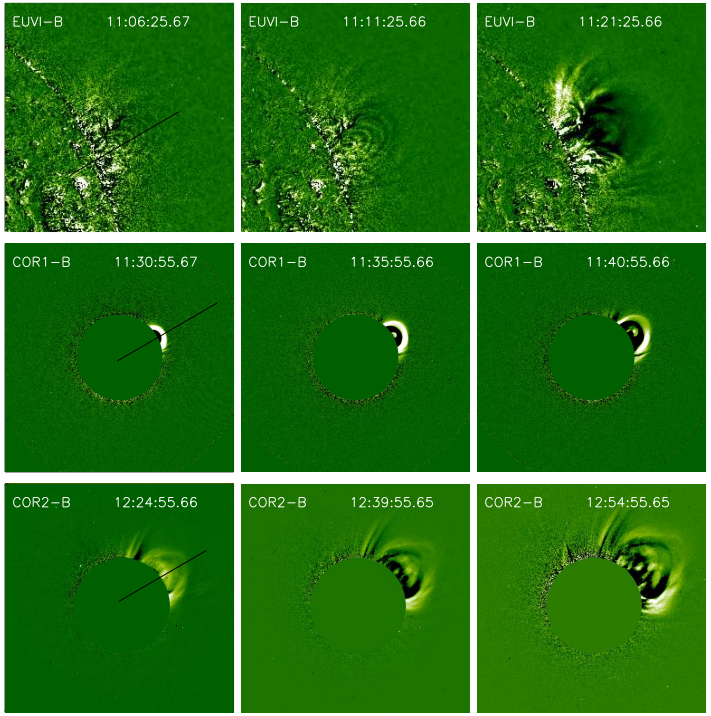

Dimming tracks the CME evolution and flare reconnection.
Significant dimming occurs at the onset of flare reconnection
(Cheng et al. 2016)

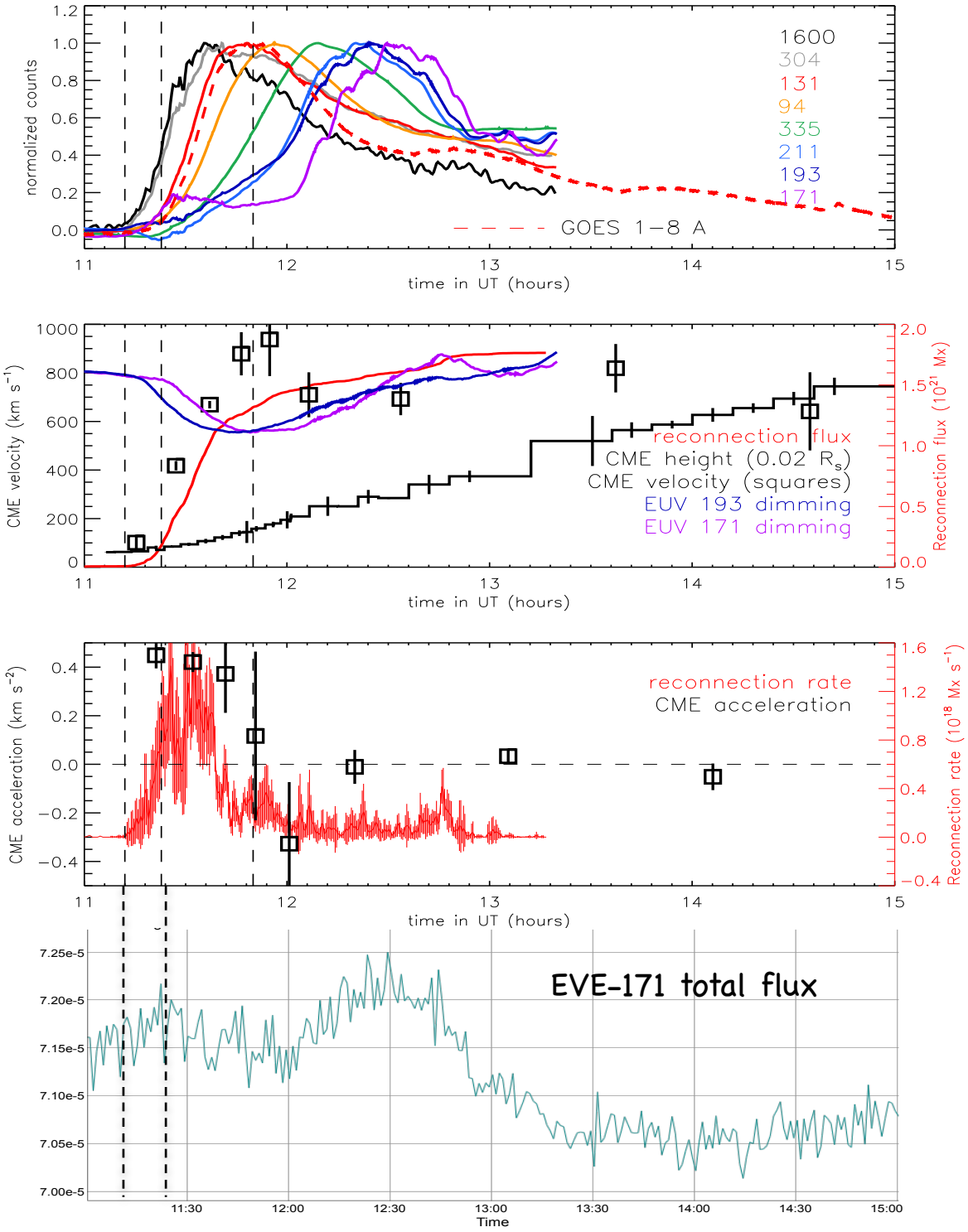

Coronal dimming and CME properties

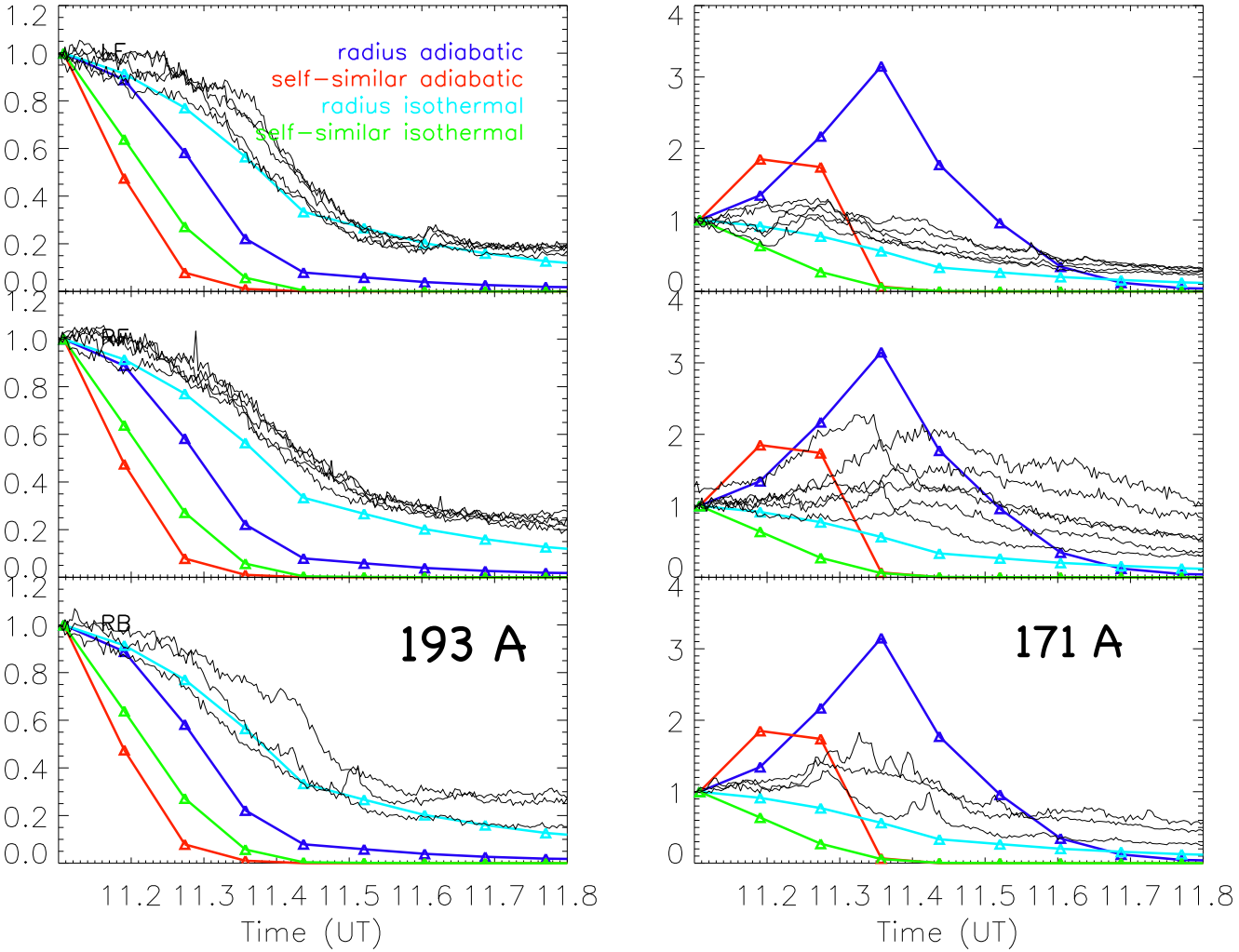

As CME rises, the emission measure (EM) decreases, and the corona becomes dimmer.

$$EM = \int n^2 dl$$

$$= \int \boxed{n^2 \frac{dl}{dT}} dT$$

DEM

$$I \sim \int \boxed{n^2 \frac{dl}{dT}} G(T) dT$$

$$\ln\left[\frac{I(t)}{I(t_0)}\right] \sim -\alpha \ln\left[\frac{H(t)}{H(t_0)}\right]$$

Coronal dimming and CME properties

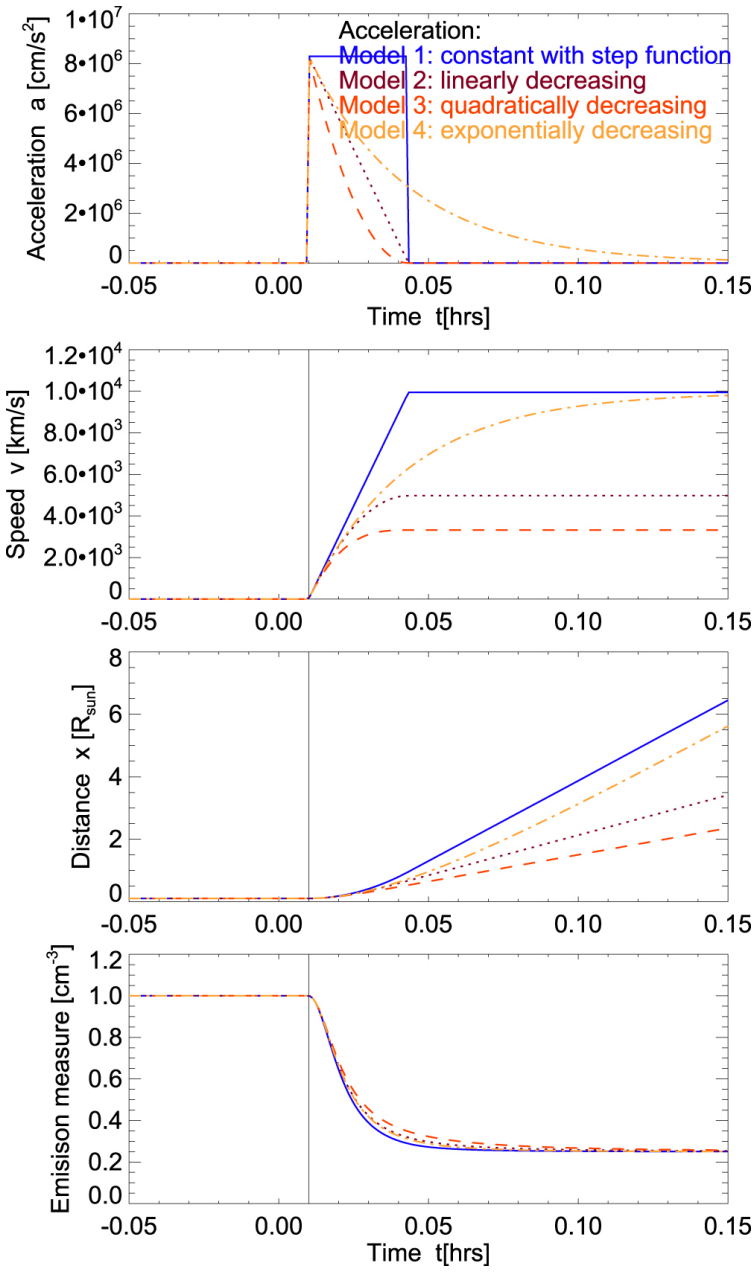

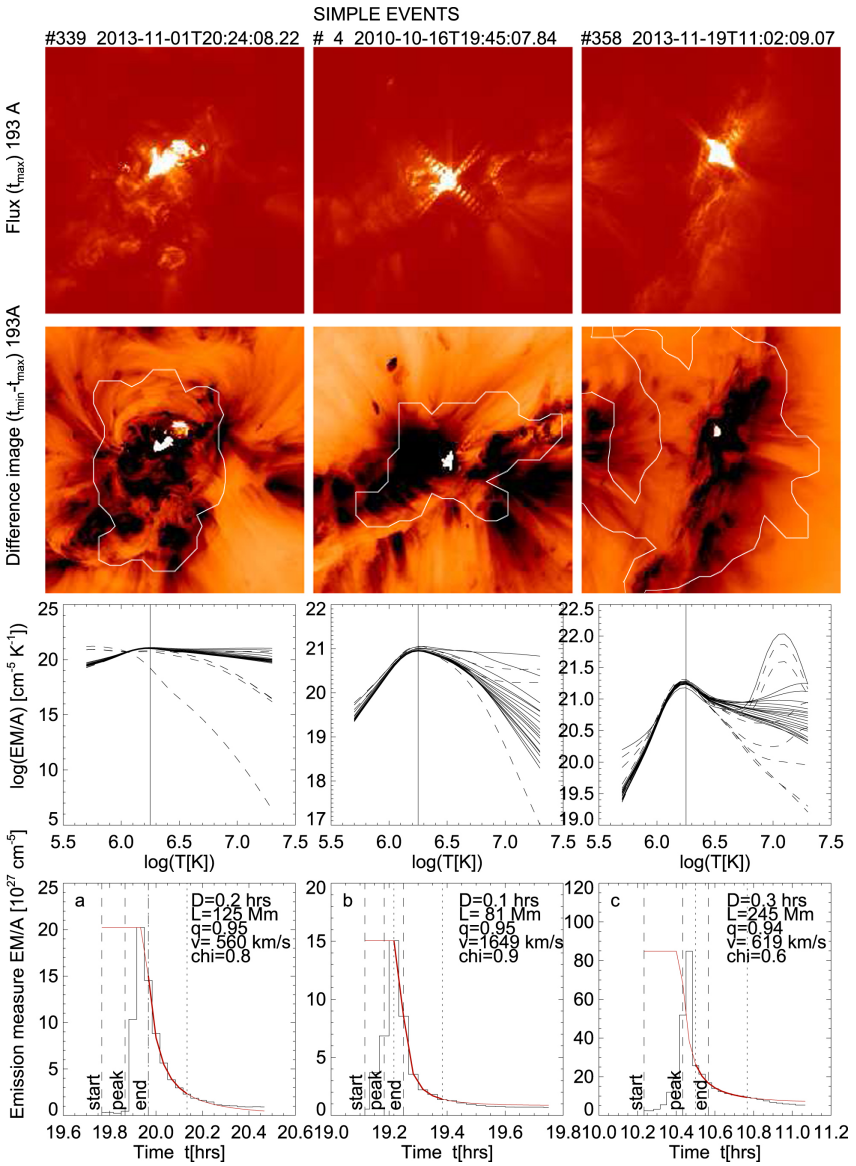

Aschwanden 2016

CME energetics with dimming analysis

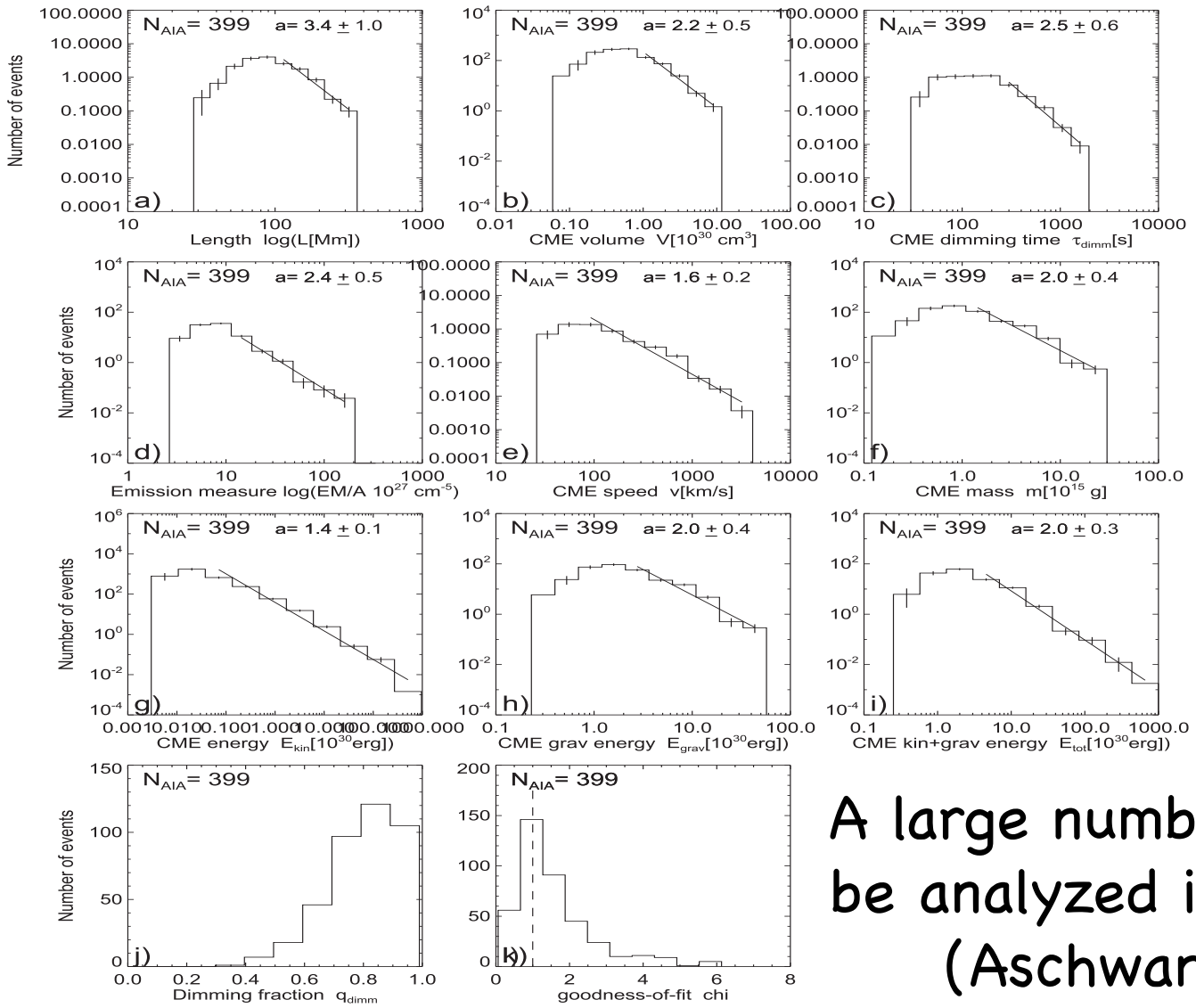

A large number of events can be analyzed in SDO era. (Aschwanden 2016)

Figure 16. Log–log histograms of various physical parameters measured from the 399 CME events based on AIA/*SDO* data. Power-law fits are applied on the right-side tails of the distributions.

CME energetics with EUV and WL obs.

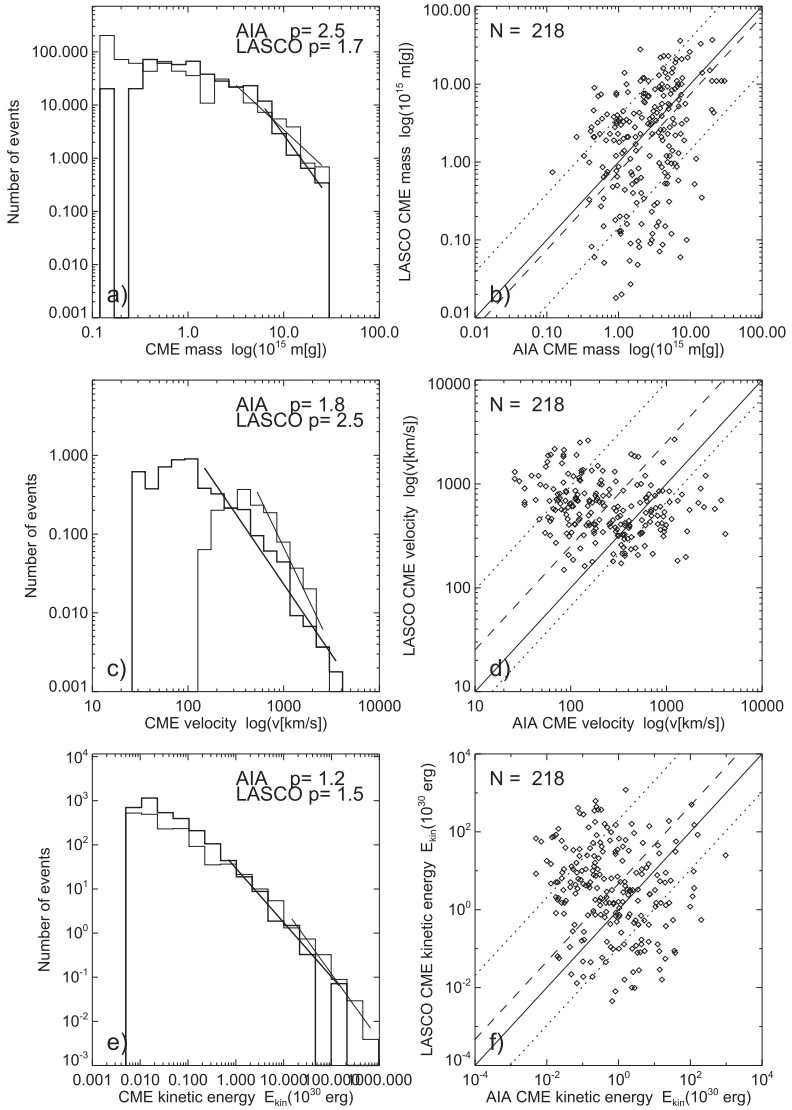

Figure 18. Comparison of of CME masses (top panels), CME velocities (middle panels), and CME kinetic energies (bottom panels) between AIA and LASCO data sets, in form of (log–log) size distributions (left panels) and scatterplots (right panels). The diagonal solid line indicates identity, along with the means (dashed line) and standard deviations (dotted lines) of the logarithmic ratios.

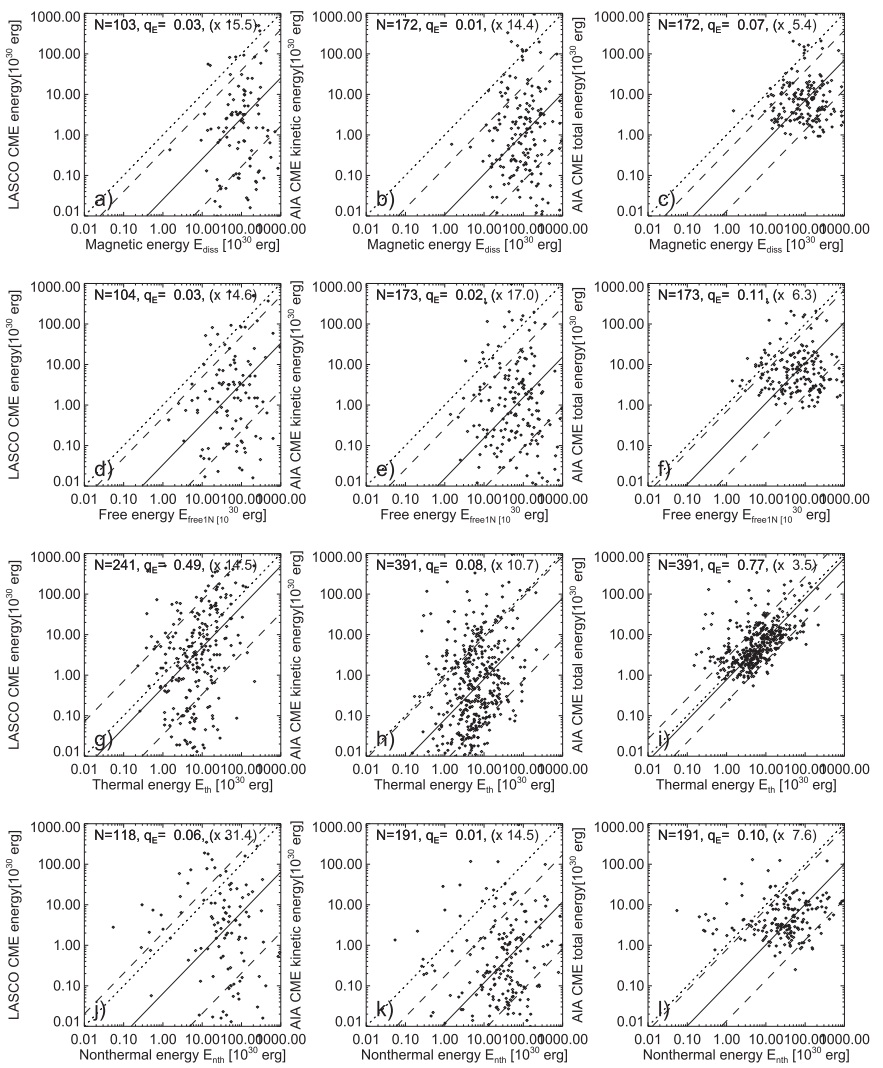

Figure 20. Scatterplot of CME kinetic energies vs. the dissipated magnetic energy (top row), the free (magnetic) energy (second row), the multithermal energy (third row), and the nonthermal energy (bottom row), for both LASCO/C2 (left column) and AIA observations (middle column). The total (kinetic and gravitational) energies are shown in the right column. Equality (dotted diagonal line), the mean (dashed line) and standard deviation (dotted line) of the energy ratios are indicated.

(Aschwanden 2016)

Summary

- CME energy from coronagraph WL observations and EUV dimming observations
- Timing of CME acceleration, flare emission, and magnetic reconnection